Reviews in Mineralogy & Geochemistry
Vol. 87 pp. XXX-XXX, 2021

Space Weathering At The Moon

Brett W. Denevi[1], Sarah K. Noble[2], Roy Christoffersen[3], Michelle S. Thompson[4], Timothy D. Glotch[5], David T. Blewett[1], Ian Garrick-Bethell[6], Jeffrey J. Gillis-Davis[7], Benjamin T. Greenhagen[1], Amanda R. Hendrix[8], Dana M. Hurley[1], Lindsay P. Keller[3], Georgiana Y. Kramer[8], David Trang[9]

[1]Johns Hopkins University Applied Physics Laboratory
11100 Johns Hopkins Road, Laurel, Maryland, 20723, U.S.A.

Brett.Denevi@jhuapl.edu, david.blewett@jhuapl.edu, benjamin.greenhagen@jhuapl.edu, Dana.Hurley@jhuapl.edu

[2]NASA Headquarters, 300 Hidden Figures Way, SW
Washington, District of Columbia, 20546, U.S.A.

sarah.noble-1@nasa.gov

[3]Jacobs, Mail Code XI3, Astromaterials Research and Exploration Science
NASA-Johnson Space Center, Houston, Texas, 77058,U.S.A.

roy.christoffersen-1@nasa.gov, lindsay.p.keller@nasa.gov

[4]Department of Earth, Atmospheric, and Planetary Sciences,
550 Stadium Mall Drive, West Lafayette, Indiana, 47907,U.S.A.

mthompson@purdue.edu

[5]Department of Geosciences, Stony Brook University,
Stony Brook, New York, 11794, U.S.A.

timothy.glotch@stonybrook.edu

[6]Department of Earth and Planetary Sciences, 1156 High Street,
University of California, Santa Cruz, California, 95064, U.S.A.

igarrick@ucsc.edu

[7]Department of Physics, MSC 1105-109-02, One Brookings Drive,
Washington University in St. Louis, St. Louis, Missouri, 63130, U.S.A.

j.gillis-davis@wustl.edu

[8]1700 E Fort Lowell Rd STE 106, Planetary Science Institute,
Tucson, Arizona, 85719, U.S.A.

ahendrix@psi.edu, gkramer@psi.edu

[9]School of Ocean and Earth Science and Technology
2525 Correa Road, Honolulu, Hawai'i, 96822, U.S.A.

dtrang@higp.hawaii.edu

1. INTRODUCTION

The Earth is cradled in an atmosphere that burns up small impactors before they reach the surface, and a magnetosphere that largely shields the surface from solar and cosmic particle radiation. The Moon and other airless planetary bodies lack such protection, and their surfaces, laid bare to the space environment, continually interact with, and are altered by this environment.

1529-6466/21/0087-00xx$05.00 (print)
1943-2666/21/0087-00xx$05.00 (online)
http://dx.doi.org/10.2138/rmg.2021.87.XX

Large impacts have shaped the terrain of the Moon, leaving a cratered surface covered with fragmental debris or regolith. At the smaller scale, each grain of regolith is likely to show damage tracks from high-energy cosmic rays, have a surface transformed by exposure to the solar wind, and be coated with vapor deposits from micrometeoroid impacts. New regolith particles are created when impact melt glass bonds together older regolith grains into particles called agglutinates. This collection of processes, through which the space environment alters the Moon's surface, is known as space weathering.

The chemical and physical changes to the surface that result from space weathering processes are known as maturation—a surface is more mature if it has experienced more space weathering. These changes also affect the way that light is absorbed and reflected by mature surfaces on the Moon and other airless bodies. The effects of space weathering are on spectacular display in crater rays, where bright immature regolith, newly exposed on the surface, stands in stark contrast to the weathered background (Fig. 1). The idea that high-reflectance rays belong to only the youngest impact craters, and are therefore ephemeral, has been around since before the space age (e.g., Gold 1955). With telescopic and eventually spacecraft observations that expanded observations into the near-infrared, it was clear that compared with high-reflectance rays, the mature lunar surface is not only darker, but also redder (i.e., more steeply increasing reflectance with increasing wavelength) and exhibits reduced contrast in absorption bands (e.g., Adams and Jones 1970; Hapke et al. 1970; Fischer and Pieters 1994; Hawke et al. 2004) (Fig. 2). New measurements at other wavelengths also exhibit measurable differences depending on a surface's maturity.

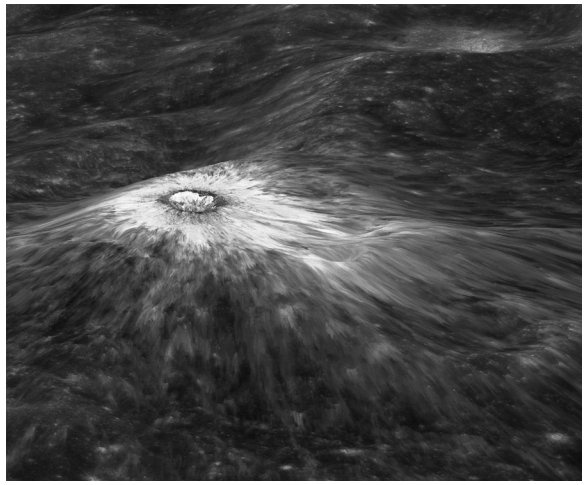

Figure 1. An oblique view of the high-reflectance ejecta and rays of a fresh impact crater (1400 m in diameter) on the Moon at 4.079°S, 151.682°E. Space weathering will alter the immature material exposed by this impact crater until its reflectance matches that of its lower-reflectance mature surroundings. LROC NAC image M1196739735LR.

Linking these changes in the remote appearance of mature lunar surfaces to specific chemical and physical changes in the regolith, and linking those chemical and physical changes to discrete space weathering processes is part of an ongoing, decades-long pursuit. For example, it was recognized early on that small particles of iron metal could be responsible for the spectral properties of mature lunar regolith, and could be deposited from a vapor phase produced by micrometeoroid bombardment or solar wind sputtering (Hapke et al. 1975). However, such vapor deposits were not actually observed in lunar samples until technological improvements enabled imaging of the nanometer-sized particles in thin (60–200 nm thick)

coatings on soil particles many years later (Keller and McKay 1993; Keller and Clemett 2001). Understanding such relationships between the spectral properties of mature soils and the space weathering processes responsible for those properties has enabled remote sensing data to be used profitably to provide insight into the degree of space exposure, to estimate surface ages, to better understand the composition of the Moon and other Solar System bodies, and to understand space weathering synoptically.

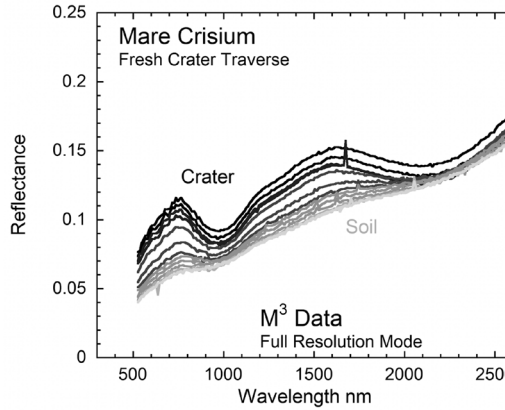

Figure 2. Moon Mineralogy Mapper (M^3) data of a traverse across a fresh crater in Mare Crisium. Traveling across a fresh impact crater demonstrates the systematic effect of space weathering: the background soil is lower in reflectance and redder (steeper spectral slope) with reduced absorption bands compared to the fresh material exposed by the impact (modified from Noble and Pieters 2016).

In this chapter we summarize the substantial recent progress in understanding space weathering that has occurred through technical innovations in the laboratory and in space, including employment of ultra-high-resolution imaging of lunar samples, a wave of new remote sensing observations, samples returned from asteroid regolith, and new methods for simulating space weathering to gain insight into its mechanisms. The chapter begins with a summary of space weathering processes and their observed effects on lunar samples (Section 2). It then describes new insights gleaned from remote sensing at a broadened range of wavelengths (Section 3.1) and from observations of special lunar environments where space weathering inputs vary, such as the intensity of solar wind at lunar swirls or in permanent shadow in polar regions (Section 3.2). We then outline how laboratory simulations have informed the understanding of space weathering mechanisms and rates (Section 4). Finally, we discuss the integrated observations and simulations and the current state of our knowledge (Section 5) and make suggestions for future investigations (Section 6).

2. SPACE WEATHERING PROCESSES AND THEIR MANIFESTATION IN LUNAR SAMPLES

Over 50 years of accumulated evidence from lunar sample and remote sensing studies has shown that the two main categories of processes that drive lunar space weathering are radiation effects, coming mostly from solar energetic charged particles, and small-scale hypervelocity impacts from micrometeoroids. Whereas contributions from other types of space environmental effects may play a role, including those from cosmic radiation sources outside the Solar System and/or from larger-scale meteoroid impacts, the significance of these other processes is still being investigated and debated (e.g., Hapke 2001).

As the characterization of space weathering products in lunar samples, particularly regolith, has progressed, it has become apparent that it is the interactive effects from small-scale impacts combined with solar ion radiation that are likely to be responsible for some of the most complex, and as yet not fully understood, space weathering products in the lunar regolith. One of the most referred-to examples of these synergistic products are the sub-micron or "nanophase" particles of metallic/reduced iron in the regolith that are now known to play a major role in determining the optical reflectance properties of the lunar surface (Hapke 2001). Iron particles are produced through high-temperature melting and vaporization that result from micrometeoroid impacts, and have been hypothesized to form through sputtering effects via solar wind irradiation. In addition, implanted solar wind H ions may accelerate the formation of Fe particles through impact-generated reduction processes. The challenges to date in validating this model by sample analysis, modeling, and/or experiment have been substantial, however, and reflect many of the difficulties in understanding space weathering at the process level. Such Fe particles are referred to in the literature by several names including: nanophase Fe (npFe or $npFe^0$), submicroscopic Fe (SMFe), Britt-Pieters (B-P) particles, optically active opaque particles (OAOpq) and others. Many of these terms carry size (submicroscopic > 40 nm <1 μm) or compositional ($npFe^0$ are metallic Fe particles) implications. In this chapter, we use nanophase Fe (npFe) as a catch-all term for Fe-bearing particles formed through space weathering processes.

In this section we review the status of the current understanding of how solar energetic charged-particles and small-scale hypervelocity impacts act both individually and in combination to drive space weathering on the Moon. A key conceptual approach taken here is one of inputs and outputs; the inputs being supplied by the Moon's space environment and surface conditions (e.g., lack of an atmosphere or planet-wide magnetic field) and the outputs being the physical, chemical, and solid-state mineralogic products that are produced by this environment and its effects.

2.1 Energetic charged-particle radiation

2.1.1 The lunar radiation environment. The Sun is the main source of the energetic charged particles (hereafter referred to interchangeably as ions but some may be neutrals) that reach the lunar surface. Superimposed on this flux of solar-sourced particles are highly energetic galactic and extra-galactic cosmic rays (GCR/EGCR), that come from distant stellar sources such as supernova explosions (Simpson 1983). No current global lunar magnetosphere or atmosphere exists to prevent any of these particles from reaching the lunar surface, but spatial and temporal variations do occur, depending on particle energy, from factors such as topography, crustal magnetic anomalies, and interactions with the Earth's magnetotail (see Section 3.2).

The flux-versus-energy spectrum of particles coming from the Sun is dominated by the solar wind at low energies (generally 1–100 keV/nucleon) with a transition to particles coming from coronal mass ejections (CME), solar flares, and other higher-energy solar events occurring above this energy range (Johnson 1990; Hundhausen 1972; Kennel et al. 1979). The flux-versus-energy spectrum of the latter higher-energy particles is a complex function of solar source, time, and solar cycle that is still being actively researched; it is centered on the 10–100 MeV/nucleon range with tails extending to overlap with the solar wind at the low end, and up to 10 GeV/nucleon at the high end (Smart and Shea 1985; Gosling 1993; Reames 1999). The flux versus energy spectrum of the solar wind has likewise been extensively studied, most recently using observations from the Genesis and Acceleration, Reconnection, Turbulence and Electrodynamics of the Moon's Interaction with the Sun (ARTEMIS) missions, and shows only second-order variations around a value of approximately 2×10^8 ions cm^{-2} s^{-1} integrated across all relevant energies and ion compositions (Poppe et al. 2018, Reisenfeld et al. 2018). It is notable that this value significantly exceeds the time averaged/energy integrated flux of particles in the higher-energy solar regime by a factor of approximately 10^4 (Johnson 1990). The relative abundances of ion species in the solar wind as well as in the higher-energy

solar particles both broadly reflect that of the Sun, with H and He dominating over heavier elements by several orders of magnitude (Johnson 1990). But complexities and unknowns abound in these relations, mostly for the higher energy particle events. For the solar wind, the typically reported relative ion abundances, which were also recently studied by the Genesis and ARTEMIS missions, are H (~96%), He (~3%) with higher-atomic number species making up the remaining fraction (Poppe et al. 2018; Reisenfeld et al. 2018; Johnson 1990).

The contribution of energetic charged particles to the lunar surface made by the GCR/EGCR flux overlaps somewhat at its lowest range of energies with the solar-sourced spectrum, but is otherwise notable for containing particles that extend to extreme energies from 1 to over 1000 GeV/nucleon. Relative ion compositions are again dominated by H (~87%), He (~12%) and ~1% heavier nuclei (Simpson 1983). The GCR/EGCR flux-versus-energy spectrum is modulated by a strong anti-correlated influence from solar activity, but the time-averaged, energy-integrated H flux is on the order of 4 H ions cm^{-2} s^{-1} (Prettyman 2014).

2.1.2 Overview of effects produced. Current understanding of the role played by solar system energetic charged particles in space weathering comes from observations made on lunar samples, laboratory experiments, and computer modeling of ion–solid interactions. Three broad categories of ion–solid interactions play a role in lunar space weathering. The first is ion implantation, in which energetic ions enter a solid to be retained once their kinetic energy is completely transferred to the target material and they come to a stop. The second category is the displacement of atoms internally within the target material due to energetic/collisional interactions with the implanting ion. The third category is ion sputtering, in which collisional interactions (or in some cases electronic excitations) cause near-surface atoms to be ejected from the host solid.

Essentially all ions across the entire flux-versus-energy spectrum of solar and extra-solar particle radiation have sufficient kinetic energy to penetrate into grains on the lunar surface to become implanted. Although some incoming ions may undergo back-scattering and not become implanted, the fraction of these particles is relatively minor (Johnson 1990). The intrinsic depths of implantation of solar ions varies from 10–200 nm for the solar wind, a few mm up to several cm for higher energy regime solar particles, and cm and above for GCR/EGCR ions (Johnson 1990). Elemental concentrations and isotopic ratios of implanted solar ion species in individual lunar regolith grains are known from only a few studies, which concentrated on minerals such ilmenite that were considered to be more "retentive" of implanted species compared to silicates (e.g., Nichols et al. 1994). In addition to implanted concentrations measured on individual grains, the concentration of implanted solar wind species, specifically H, have also been measured on bulk lunar regolith samples (Gibson and Bustin 1988; Bustin et al. 1984, 1986). The results show H concentrations in the range of 10–80 μg/g that appear to be well-correlated with soil maturity. The bulk soil data are notable for providing a potential means to understand how implanted solar species are re-processed, re-distributed or removed from the bulk soil by dynamic mixing and heating linked to micrometeoroid impact and other thermal events.

As an ion becomes implanted in a solid, it can drive space weathering by virtue of its ability to collisionally displace atoms in the target crystal, thereby driving a range of processes that alter the crystal's structure and composition (Johnson 1990; Wang and Ewing 1992). These displacements can occur by various combinations of nuclear-elastic collisions, also called nuclear stopping, and transfer of energy to excitations of the solids' electrons, or electronic stopping (Johnson 1990; Wang and Ewing 1992). For ions with total energies in the range of the solar wind, nuclear-elastic interactions dominate such that the collisional damage efficiencies for solar wind H and He reach a maximum near the 1 keV/nucleon average solar wind energy, falling off towards higher energies (Johnson 1990). For ions in the higher-energy solar and extra-solar regime, the diffuse transfer of energy mostly to a solid's electron cloud is only able to accomplish significant atomic displacements for ions with atomic numbers equal

to or greater than the transition elements, and only in a window of energies centered at ~1 MeV/nucleon (Fleischer et al. 1975). The damage that each ion creates in this case is highly efficient, but also localized on the nanoscale, leading to the formation of linear damage tracks in crystalline solids measuring only a few nanometers wide (Fleischer et al. 1975) (Fig. 3a, b).

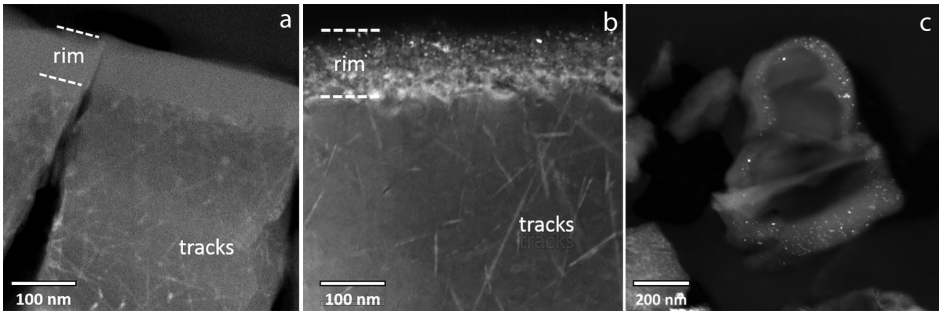

Figure 3. Darkfield transmission electron microscope (TEM) images of lunar soil grains. **a)** ~100-nm solar wind amorphized layer on an anorthite grain from sample 62231. The bright linear features in the core of the grain are solar flare particle tracks. **b)** Solar-wind damaged rim on an olivine grain from sample 71501. In contrast to the anorthite grain, the rim is not amorphous but nanocrystalline and contains nanophase iron (white specks) that formed in situ (Keller and Berger 2014). Abundant solar flare tracks are also visible. **c)** Vapor-deposited rim on an anorthite grain from 79221. The bright spots are nanophase iron particles.

The first observations of ion damage effects in lunar regolith grains from solar wind ion exposure were made by early post-Apollo transmission electron microscope (TEM) studies (Dran et al. 1970; Bibring et al. 1974; Borg et al. 1971, 1980). These reported circumferential amorphous rims 10–150 nm thick, most typically on small (<40 μm) grains of lunar plagioclase, but also on other minerals. The width of the rims was consistent with the expected penetration range of solar wind ions, demonstrating for the first time that under sufficiently long solar wind exposure, a grain's outer margins could accumulate enough ion damage to undergo ion-induced amorphization (the loss of periodic crystalline structure; Bibring et al. 1974). As TEM studies progressed from this early work, new discoveries uncovered several levels of complexity in the microstructure and origin of the rims. Using TEM micro-chemical analytical capabilities, Keller and McKay (1993, 1997) showed that many rims were composite in nature, containing outer layers that were very different in major element composition and microstructure from underlying amorphous ion-damaged layers. The distinct composition indicated the layers were depositional, and they were found to contain high modal concentrations of spherules of metallic Fe 1–10 nm in diameter with commensurate compositional enrichments in Fe as well as volatile elements such as S and Na (Keller and McKay 1993, 1997).

The Keller and McKay (1993, 1997) TEM imaging studies amounted to a confirmation of early suggestions from Apollo-era surface analytical and other studies that optically-dark, Fe-rich coatings were present on many lunar regolith grains. Although these earlier studies lacked full details on the nature of the coatings, several possible origins were nevertheless proposed and investigated experimentally (Hapke 2001). In most cases the postulated origins were discussed in the context of "vapor deposition" with the vapors being derived from solar wind ion sputtering or impact vaporization of neighboring regolith grains. Keller and McKay (1993, 1997) favored an impact vapor deposition origin based on the deposits' compositional enrichment of volatile elements, such as S and Na. Other arguments in favor of solar wind sputter deposition were presented (Hapke et al. 1994), with the result that some uncertainty has remained in the space weathering research community about how the deposits are produced (see Section 5.2.2).

Following their confirmed discovery by TEM, the deposited outer layers of npFe on regolith grains garnered considerable interest because of their implications for remotely-sensed optical reflectance properties (Section 3). At the same time, interest waned somewhat in the non-deposited portion of grains rims formed due to solar wind ion effects. Ongoing TEM studies did nevertheless reveal that not all lunar minerals respond to solar wind ion irradiation the same way, with minerals such as olivine and ilmenite showing ion-damaged rims with complex, highly-defective microstructures that were not fully amorphous (Christoffersen et al. 1996; Keller et al. 2021). Incremental studies have attempted to better understand these differences with an eye to using variations in ion damage effects as a way to estimate the regolith surface exposure history of individual grains (Keller et al. 2021).

2.2 Micrometeoroid impacts

2.2.1 The lunar micrometeoroid environment and small-impact flux. Micrometeoroids, particles in the size range of ~tens of nanometers to hundreds of micrometers (size distribution peaks near 220 μm), are thought to be one of the key agents of space weathering. The Moon is bathed in a rain of micrometeoroids that strike the lunar surface at rates that average to approximately one per square meter per day (Love and Brownlee 1993; Vanzani et al. 1997; Grün et al. 2011). In contrast to the Earth, where micrometeoroids burn up in the atmosphere, micrometeoroids reach the surface of the Moon constituting hypervelocity impacts with the lunar regolith. Thus, the composition, mass distribution, relative velocity, and spatial distribution of the micrometeoroids are important factors for space weathering. The "Dust, Atmospheres, and Plasma" chapter (Farrell et al. 20XX, this volume) provides more information about the meteoroid environment around the Moon, including observations by the dust detector onboard the Lunar Atmosphere and Dust Environment Explorer (LADEE) (e.g., Horanyi et al. 2015).

The micrometeoroid environment consists of a background of "sporadic" meteoroids superposed by "meteor streams," which are short, more intense enhancements that occur at the same time each year. These micrometeoroids originate from multiple sources. Jupiter-family comets are estimated to be the source of >85% of micrometeoroids, with <10% coming from asteroids and <10% from long-period comets (Nesvorný et al. 2010). The orbits of dust sourced from Jupiter-family comets are circularized by Poynting–Robertson drag by the time the dust grains reach the Moon, resulting in mean impact velocities that are only modestly higher than dust sourced from asteroids (~14.5 km/s vs. 12.5 km/s; Nesvorný et al., 2010). However, the full distribution of micrometeoroid impact velocities encompasses substantially higher values (e.g., Campbell-Brown 2008; Nesvorný et al. 2011; Pokorný et al. 2014).

The spatial distribution of the incident micrometeoroid flux is not isotropic owing to the orbital characteristics of the source populations. The peak micrometeoroid flux occurs in the apex direction, or the direction of the Earth–Moon system's orbit around the Sun (Jones and Brown 1993). However, there are also lesser clusters of incident flux associated with the helion and toroidal populations (e.g., Jones and Brown 1993; Campbell-Brown 2008; Pokorný et al. 2014). While the apex/anti-apex and helion/anti-helion populations are concentrated at low latitudes, the toroidal populations are concentrated at high latitude.

2.2.2 Overview of effects produced. Micrometeoroid impacts at the velocities experienced on the Moon result in substantial melting and vaporization of target soil particles (e.g., Cintala 1992). Because a portion of the vapor and melt created by micrometeoroid (and larger) impacts is not just retained within the crater, but deposited onto the surfaces of nearby soil grains, this process also results in the creation of thin, amorphous rims coating regolith particles. Vapor and melt deposited rims created from micrometeoroid impacts can be distinguished from the amorphous solar wind damaged rims described above when there is a compositional contrast between the underlying grain and the rim (though of course coatings of similar composition can occur). As described above, such rims typically contain npFe particles (Fig. 3c), which

are thought to form by solid-state condensation from the high-temperature vapor. In the vapor cloud the Fe–O bonds are weak and the sticking coefficient of O on adjacent surfaces is low, resulting in the condensation of reduced, Fe-rich deposits. Similarly, npFe particles can form from melt through silicate–metal liquid immiscibility (Housley et al. 1973).

Substantial effort has been undertaken to confirm that the spectroscopically important npFe is produced via micrometeoroid impacts. Because such high velocity impacts are difficult to reproduce in the laboratory, pulsed laser irradiation is often used to simulate the short-duration high-temperature characteristics of such events (Section 4.1). However, recent work has provided direct views of microcraters, with diameters as small as 8 μm, that formed in lunar rocks on the Moon and were subsequently returned to Earth by Apollo astronauts. Focused Ion Beam (FIB) techniques have been used to produce cross sections of three such microcraters, yielding new views of the effects of micrometeoroid bombardment (Fig. 4; Noble et al. 2016). In these microcraters, an impact melt lining ranging from glassy to polycrystalline with the same composition as the host grain was found to overlie a shocked and fractured zone. Whereas no nanophase inclusions were identified in a crater formed in plagioclase, npFe was found within the melt of a crater formed in olivine, and a thin npFe-rich layer superimposed on the melt lining, interpreted to be a vapor deposited layer, was found in the craters that formed in both olivine and pyroxene (Fig. 5). The npFe in both samples was consistent in size, ~3–7 nm diameter (Fig. 5), similar to the size ranges found in soil rims (Noble et al. 2016).

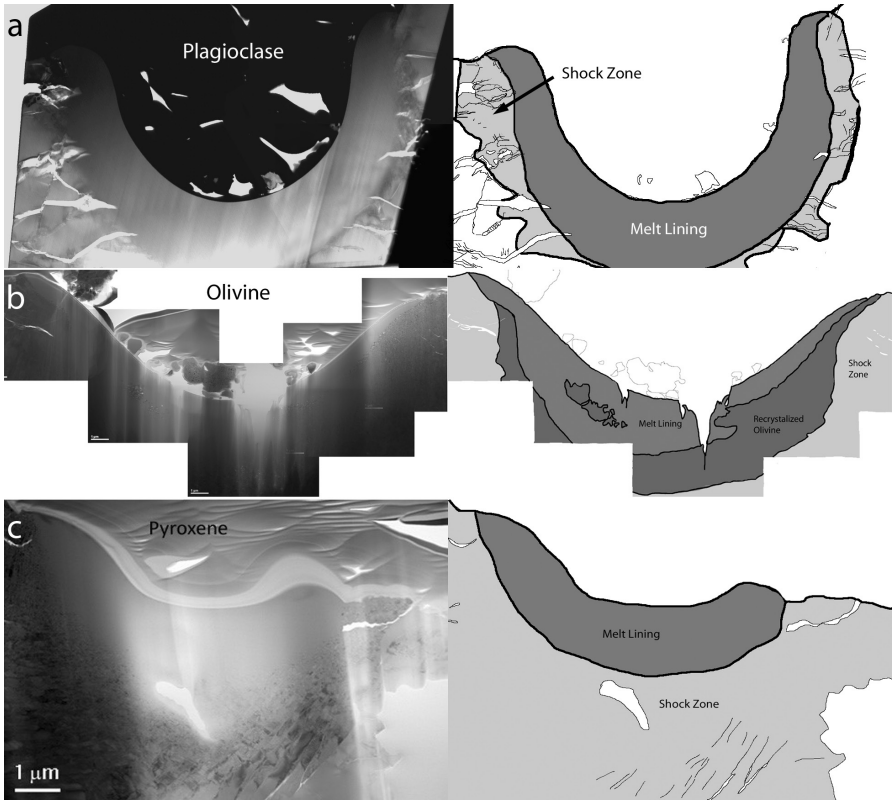

Figure 4. TEM images of cross sections through micro-scale impacts into **a)** plagioclase (crater diameter 10 μm), **b)** olivine (crater diameter 18 μm), and **c)** pyroxene (crater diameter 8 μm). Corresponding sketch maps of each micro-scale impact are also shown.

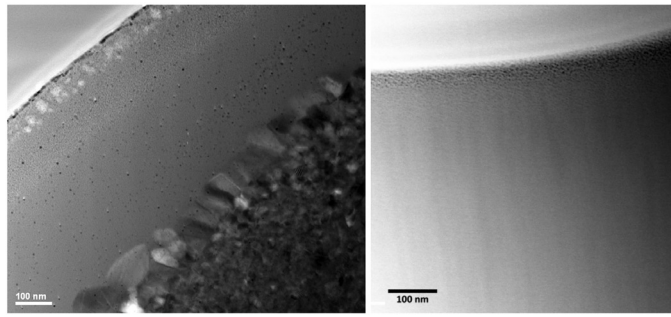

Figure 5. TEM images of npFe in olivine, and pyroxene craters. NpFe (black specks) is abundant throughout the olivine glass on the left, but only at the uppermost surface in the pyroxene sample on the right.

Micrometeoroid impacts have several other key effects distinct from those of the solar wind. One such effect is the creation of agglutinates, regolith particles that are produced when glasses created by micrometeoroid impacts weld other mineral and regolith fragments together (Fig. 6). In mature regolith, and thus across most of the Moon's surface, 40–60% of the regolith is comprised of agglutinates (McKay and Basu 1983). Agglutinates have distinct physical properties—they are highly irregularly shaped and vesicular (Fig. 7), and dark in the visible wavelengths. Agglutinates also contain a high abundance of npFe particles that are distributed in the glass throughout the volume of the agglutinate rather than restricted to the uppermost surface (Fig. 7b). These iron particles span a much wider range of sizes (up to hundreds of nanometers in diameter; James et al. 2002; Basu 2005) compared to the iron particles within the rims on individual regolith grains (~1–10 nm in diameter; Keller and Clemett 2001). The details of the formation mechanism(s) of these iron particles are still being investigated (Section 5.2.1).

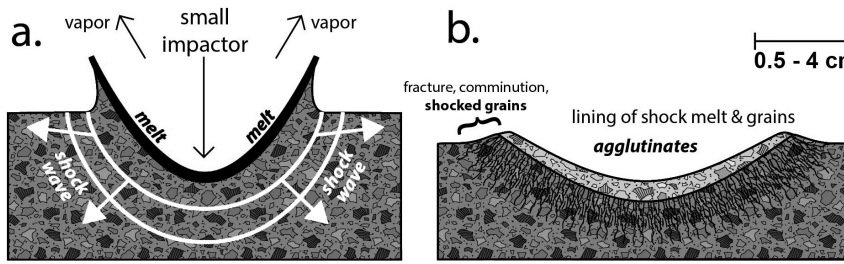

Figure 6. Schematic illustration of a small-scale impact event generated by a mm- to sub-mm size impactor into fine-grained lunar regolith. **a)** Mid-impact stage processes and products include shock wave generation, formation of shock melt and vapor. **b)** Post-impact products are impact melt mixed with grains to form agglutinates and comminuted/shocked solid grains. Crater diameter shown would typically be in the range of 1–4 cm.

The abundance of iron particles within agglutinates means that they have relatively high magnetic susceptibility and can be, to some degree, magnetically separated from other regolith components (e.g., Adams and McCord 1973; Morris 1977; Denevi et al. 2020). The relative abundance of npFe particles in lunar regolith can be measured using ferromagnetic resonance (FMR) techniques, which detect single-domain, metallic particles <30 nm in size (Housley et al. 1974; Morris 1976, 1978, 1980). Measured as IS, this parameter is typically normalized by the FeO content of the regolith, creating a maturity parameter, IS/FeO that is largely independent of composition. IS/FeO has been widely used to classify regolith as immature (IS/FeO < 30), submature (IS/FeO > 30 to < 60), or mature (IS/FeO > 60) (Morris 1976), and this sample-based maturity parameter correlates to those based on spectral reflectance (Section 3.1).

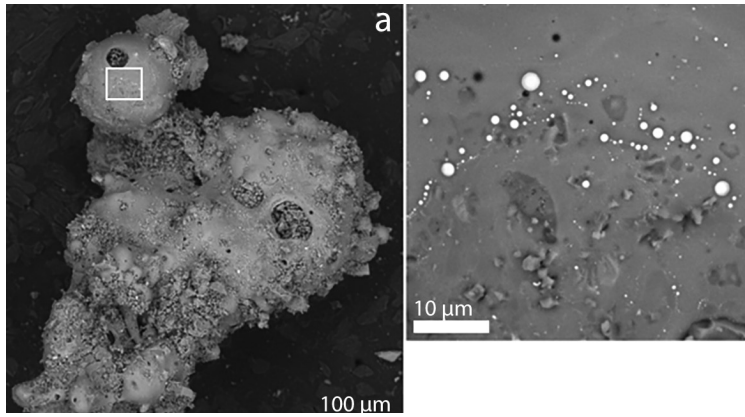

Figure 7. SEM image of an agglutinate from sample 15041. **a)** Morphology of agglutinate, where smoother patches are glass that welds together other soil fragments. The area shown in panel b is indicated with a white box. **b)** Microphase iron particles (white) extend to larger sizes than those found within grain coatings.

Although the maturity index, IS/FeO, and space weathering studies of lunar regolith are focused on the abundance of reduced, metallic iron (i.e., Fe^0, or $npFe^0$), it should be noted that the nanophase iron particles within agglutinates have been shown to have a mixture of oxidation states (Keller and Clemett 2001; Thompson et al. 2016; Burgess and Stroud 2017). Recent high-resolution electron energy-loss spectroscopy (EELS) measurements revealed the presence of nanoparticles in lunar regolith with variable oxidation states (Fe^0, Fe^{2+}, and Fe^{3+}), and showed that increasing oxidation state correlates with maturity, suggesting nanophase iron was initially deposited as Fe^0 and subsequently oxidized (Thompson et al. 2016; Burgess and Stroud 2017). Several mechanisms for oxidation of these nanoparticles have been proposed, including via the Kirkendall effect, whereby oxygen from the surrounding silicate matrix diffuses towards the highly reactive surface of the nanoparticle, and/or via water molecules in the lunar regolith (Thompson et al. 2016; Burgess and Stroud 2017). Less than 15% of all nanoparticles measured across all regolith samples in Thompson et al. (2016) had Fe^{3+} in proportions >25%. At these abundances, radiative transfer modeling indicates that oxidized iron does not substantially affect the spectral properties of lunar regolith (Thompson et al. 2016).

Finally, we note here that small impact events, together with secondary impactors created from the ejecta of larger impact events, also continually mix the upper layers of the lunar regolith, exposing and burying material so that a well-mixed upper layer of mature regolith forms because nearly all grains spend time at the surface (e.g., Speyerer et al. 2016; Costello et al. 2018). The critical importance of regolith gardening to space weathering is discussed further in Section 5.1.

3. REMOTE SENSING OBSERVATIONS OF THE EFFECTS OF SPACE WEATHERING

The preceding section described the space weathering processes that act at the Moon's surface, and the resulting physical and chemical changes inflicted at the very local level—namely, on individual regolith grains. Here we explore how remote observations provide further insight into space weathering by allowing comparisons across geologic features of varying ages, compositions, and environments.

Interpreting remote sensing measurements of the Moon benefits from the decades of investigations of laboratory reflectance spectra collected of returned lunar regolith samples and analogs. The result is that the differences in the visible and near-infrared spectral properties of

immature and mature regoliths are well known: mature regolith has lower reflectance, reduced contrast in crystal field absorption bands, and steeper (redder) spectral slope (e.g., Adams and Jones 1970; Hapke et al. 1970; Fischer and Pieters 1994; Hawke et al. 2004; Fig. 2). We can also attribute these spectral properties to the space weathering products described in Section 2. The conversion of crystalline material to glass—whether the amorphous rims on regolith grains or that within agglutinates—does have spectral effects: compared to mafic silicates, the crystal field absorption bands in glass are broader and shallower and result in a moderately lower overall reflectance (Wells and Hapke 1977; Denevi et al. 2008). However, the largest spectral changes are attributed to npFe particles (e.g., Pieters et al. 1993; Hapke 2001; Noble et al. 2001). The presence of these small, opaque iron particles concentrated within a more transparent silicate matrix means that a photon is much more likely to interact with an iron particle and be absorbed before interacting with a grain boundary and scattered back (e.g., Hapke 2001). Thus, the spectra of mature regolith takes on the spectral features of iron metal, while the absorption bands related to the silicates are harder to discern.

Iron particles are present in both the space weathered rims on regolith grains and within agglutinates (Section 2). Both the size and abundance of npFe affect reflectance spectra. Keller et al. (1998) suggested that larger opaque particles cause spectral darkening and that very small particles cause reddening. Noble et al. (2007) systematically explored the effects of size and concentration of nanophase iron by impregnating a series of silica gels with different pore sizes with nano- and microphase Fe particles (Fig. 8). The results agreed with and quantified the earlier observations and demonstrated that small npFe ($\lesssim 40$ nm) cause substantial reddening in the visible and darkening across the visible–near-infrared, and larger npFe particles ($\gtrsim 40$ nm) cause darkening, but not reddening, throughout the wavelength range. Updates to spectral models have proven successful for modeling the spectral effects of these different npFe grain sizes (see Section 3.1.1).

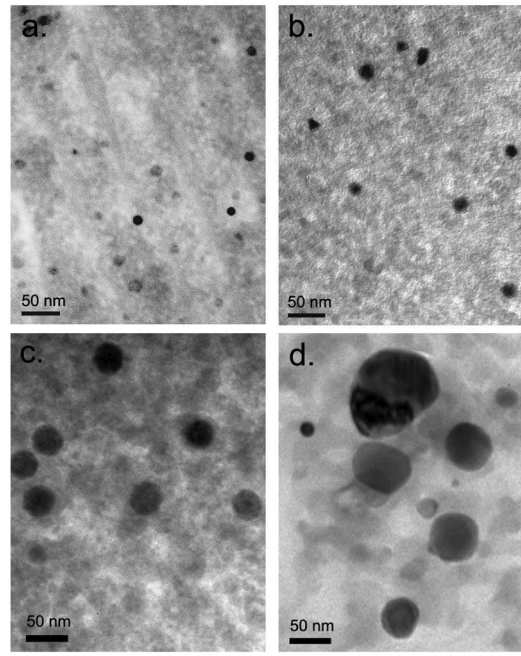

Figure 8. TEM bright field images of silica gels impregnated with nano- and microphase iron particles. The varying pore sizes of the gels results in iron particles with different sizes: **a)** 2.3 nm, **b)** 6 nm, **c)** 25 nm, and **d)** 50 nm. From Noble et al. (2007).

3.1 New observations of lunar surface maturity

For some time, remote space weathering studies were largely restricted to examining the optical variations in maturity, "optical" having been generously broadened to include visible to near-infrared wavelengths. The last decade has yielded new information about the effects of space weathering from the far-ultraviolet (UV) to thermal infrared (TIR). This expansion in our available means for observing the Moon's surface has extended our knowledge of how the processes of space weathering manifest themselves in remote observations. Many of the newest insights from these data are related to what we term "special" lunar environments—regions at high latitudes, specific longitudes, permanent shadow, and sites of crustal magnetic anomalies. Section 3.2 is devoted to these areas; the following section focuses on the results of more general maturity-related studies that have recently provided new understandings of how lunar space weathering operates.

3.1.1 Visible–near-infrared. Much of our fundamental knowledge of surface maturity has come from observations at visible and near-infrared wavelengths, and this portion of the spectrum continues to provide new information on how space weathering proceeds on the Moon.

Following the Clementine mission, an empirical parameter designed to quantify optical maturity (OMAT) was developed from values of reflectance at 750 nm and a ratio of 750 to 950 nm reflectance (Lucey et al. 2000). When applied globally, this parameter highlighted variations in maturity and largely muted compositional differences, providing a simple method for comparing relative maturity. Since that time, variations on the original OMAT parameter have sought refinements using newer datasets (e.g., Kumar and Kumar 2014; Lemelin et al. 2016a; Sun et al. 2016).

One obstacle to implementation of OMAT as a tool for global quantitative comparison is that it is not completely independent of composition (e.g., Staid and Pieters 2000; Sun et al. 2016). For example, regional and global maps of three maturity-related parameters derived from Moon Mineralogy Mapper (M3) data (reflectance at 1.6 μm, integrated depth of the mafic-mineral absorption band near 1 μm, and a reflectance ratio connected to continuum slope) demonstrated highland–mare and intra-mare differences in maturity (Nettles et al. 2011). That work advocated using such parameters for regional studies only. Other studies have compared OMAT with complementary datasets like Mini-RF circular polarization ratio observations (e.g., Cahill et al. 2014). Such presumably composition-independent parameters, which are related to roughness and larger-scale physical breakdown of materials, could also provide a means to further minimize compositional influence on OMAT.

Despite these complications, OMAT has proven useful for a wide variety of lunar geologic studies (e.g., Blewett et al. 2005, 2011; Ghent et al. 2005; Hawke et al. 2005; Giguere et al. 2006; Fa and Jin 2007; Kramer et al. 2011a; Braden et al. 2014), including efforts to understand the relative and possibly even absolute ages of individual craters (e.g., Mahanti et al. 2016) and the Copernican period as a whole (Hawke et al. 2004), and for comparisons with other bodies (e.g., Braden and Robinson 2013).

Radiative transfer modeling (e.g., Hapke 2011) provides another method to derive information about the maturity of lunar regolith from spectroscopy. When the inherent optical properties (i.e., optical constants) of component materials (minerals, glasses, iron) are known, such modeling can be used to derive their abundances from remotely obtained spectra. Previous work using the model of Hapke (2001) showed that npFe abundances derived from reflectance spectra of Apollo regolith samples were correlated to the ferromagnetic resonance (IS/FeO) of these samples (Denevi et al. 2008). However, this model was shown to be appropriate only for npFe $<$ 50 nm, not the larger "microphase" iron particles ($>$ 50 nm) (Lucey and Noble 2008); an update made use of Mie theory to more accurately represent the spectral effects of large npFe particles (Lucey and Riner 2011). Further improvements necessary for accurate

modeling of maturity came from new optical constants for metallic iron, obtained via vapor deposition of an iron film onto a fused-silica prism, with optical measurements made through the prism to minimize any influence of oxidation (Cahill et al. 2012). These developments in radiative transfer modeling have been applied to Kaguya Multiband Imager data to separately model nanophase and "microphase" iron abundance across the Moon (Trang and Lucey 2017).

The landing of the Chang'E-3 spacecraft and rover (Yutu) provided a novel opportunity to study surface maturity. Visible and near-infrared spectra were collected by the rover at various distances from the lander, within and on the edge of the area disturbed by the lander's rocket exhaust (Wang et al. 2017; Wu and Hapke 2018). The disturbed area has higher reflectance than the surroundings, as seen in pre- and post-landing images from the Lunar Reconnaissance Orbiter Camera (LROC) Narrow Angle Camera (NAC) (Clegg-Watkins et al. 2016). Comparison of the spectra with model spectra indicated that the regolith at the minimally disturbed location contains substantially higher abundance of nanophase iron than the regolith most affected by lander exhaust, suggesting removal of highly mature regolith and exposure of less mature material from deeper in the regolith.

3.1.2 Space weathering at ultraviolet wavelengths. The ultraviolet portion of the spectrum provides a relatively new tool for studying space weathering, largely because of the paucity of data previously available. Some telescopic spectra extended to wavelengths as short as 300 nm (e.g., Pieters 1977), and crater rays were noted in the UV–NIR difference images of Whitaker (1972), but only recently with instruments on the Lunar Reconnaissance Orbiter (LRO), the Lyman-Alpha Mapping Project (LAMP; 57–196 nm) and LROC Wide Angle Camera (WAC; 321–689 nm), did global UV datasets become available.

Spectra of Apollo samples provided a framework for the interpretation of LRO UV data. Comparisons of UV spectra of powdered lunar rocks (no space weathering) and mature regolith demonstrated that the UV spectral slope of mature regolith is shallower (increases more slowly with increasing wavelengths), or "bluer" (Hendrix and Vilas 2006); spectra of regolith samples across a wide range of maturity confirm this trend (Denevi et al. 2014) (Fig. 9a,b). LAMP and LROC WAC observations of young impact craters, such as Giordano Bruno, display a steeper (less blue) UV spectral slope than typical mature regolith (Fig. 9c), consistent with laboratory spectra (Hendrix et al. 2012, 2016, Denevi et al. 2014).

However, some Copernican craters identified in visible–near-infrared reflectance data show only minimal differences in their UV slope. This may be explained by the shallower penetration depth of light at shorter wavelengths, which results in the UV spectrum being more strongly affected by npFe-rich particle coatings rather than the underlying grain (Hendrix and Vilas 2006). Spectra of Apollo samples also display this trend, with the UV slope decreasing

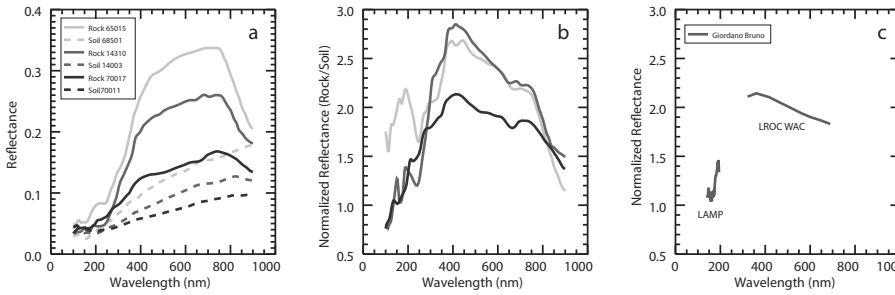

Figure 9. a) Spectra of immature materials (powdered rocks) and mature soils from the Apollo 14, 16, and 17 landing sites (data from Wagner et al. 1987). **b)** Each immature spectrum divided by the corresponding mature spectrum from the same landing site. **c)** LAMP and LROC WAC spectra of Giordano Bruno crater and its ejecta, normalized to the spectrum of mature highlands at 27.12°N, 169.81°E.

with increasing maturity up to IS/FeO values of ~40 (submature), compared to VNIR spectral variations up to IS/FeO values of ~60 (Denevi et al. 2014). Ultraviolet spectra of irradiated samples also showed differences earlier (after less irradiation) than visible–near-infrared spectra (Kanuchova et al. 2015). This interpretation also explains why UV images from the Hubble telescope showed little variation due to maturity (Robinson et al. 2007); nearly everything seen in those images is mature. Taken together these observations suggest that the UV portion of the spectrum may aid in pinpointing the freshest materials on the lunar surface, and in discriminating among ages of young Copernican craters.

3.1.3 Space weathering in the thermal infrared. Early experimental work suggested that thermal infrared observations would not be sensitive to, or affected by, the products of space weathering: no shift in the wavelength positions of spectral features was observed for crystalline vs. amorphous phases (Nash et al. 1993) and spectra of lunar samples of similar composition did not have a dependence on measured Is/FeO (Salisbury et al. 1997). Therefore, it was somewhat surprising when LRO Diviner Lunar Radiometer (Paige et al. 2010b) thermal emission observations appeared to correlate with visible–near-infrared optical maturity (Greenhagen et al. 2010).

Diviner makes use of three narrow-band channels centered near 8 μm to characterize the silicate Christiansen Feature (CF), the position of which indicates the level of silica polymerization, and therefore, composition (Logan et al. 1973, Salisbury and Walter 1989). Mature lunar surfaces exhibit CF positions shifted toward longer wavelengths compared to immature surfaces of the same composition (Greenhagen et al. 2010; Lucey et al. 2017), an observation that has been confirmed by laboratory measurements (Shirley 2018; Fig. 10) and extends to swirls (Section 2.2.1) and their surroundings (Glotch et al. 2015).

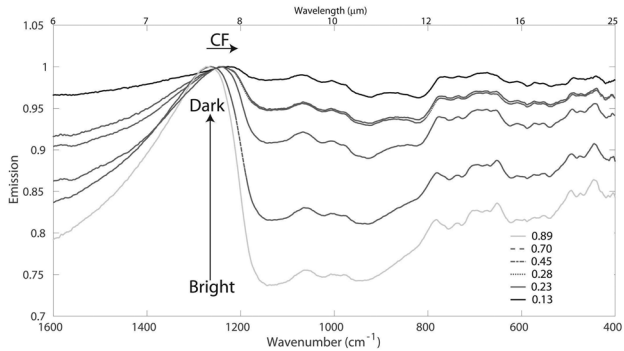

Figure 10. Thermal emission spectra of anorthite powders in a simulated lunar environment. Powders were sequentially darkened with nanophase carbon lamp black. Progressively darkened samples exhibit shifts in the CF to longer wavelengths and reduced spectral contrast. Values in the legend are sample albedos measured at 750 nm. Adapted from Shirley (2018).

A detailed comparison of lunar CF positions measured by Diviner with OMAT derived from Clementine multispectral data (Lucey et al. 2000) demonstrated that lunar surface features with low optical maturity (e.g., Copernican rayed craters and lunar swirls) show consistent CF anomalies (Lucey et al. 2017). Based on an analysis of the fresh, compositionally homogenous lower central peak of Jackson crater, a correction to mitigate the effects of space weathering on the silicate CF position was developed. The cause of the thermal infrared response to space weathering is thought to be the lower visible albedo of mature materials and resultant change in the thermal gradient in the upper hundreds of micrometers on lunar regolith (Lucey et al. 2017). This hypothesis is supported by emission spectra of olivine collected in a simulated

lunar environment (Shirley et al. 2017). When olivine powders were darkened with carbon, they showed a roughly linear correlation between CF position and albedo measured at 750 nm, demonstrating that visible albedo and related temperature gradients, in general, alter CF position.

3.1.4 Integrating information across wavelengths. The wider range of wavelengths that have now been systematically used to observe the Moon has, as described above, shown how space weathering affects the ultraviolet, visible and near-infrared, and thermal infrared (Fig. 11). These differing spectral regimes have differing sensitivities to space weathering products that reflect varying degrees of transmission and absorption as a function of wavelength.

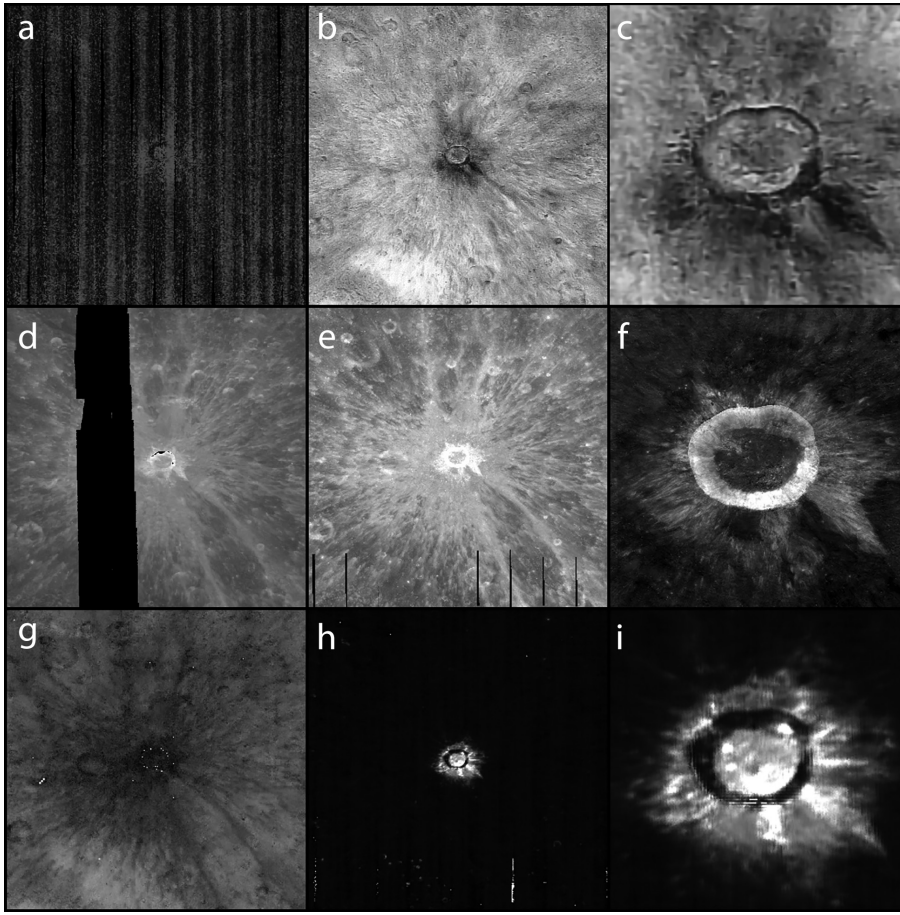

Figure 11. New views of fresh crater Giordano Bruno highlight the effects of space weathering across the spectrum. 10 × 10 degree maps of **a)** LAMP Ly-a, **b)** LROC WAC 321/415 nm ratio where low values correspond to shocked materials, **d)** Clementine OMAT, **e)** MI OMAT, **g)** Diviner CF value, and **h)** Diviner rock abundance. 2 × 2 degree detail maps are provided of **c)** LROC WAC 321/415 nm ratio, **f)** MI OMAT, and **i)** Diviner rock abundance. Note immature areas extends well beyond the areas with the highest abundances of rock and shocked materials; vertical banding in **panel a** is an artifact.

In the UV, the sensing depth is shallow (see Table 1) and the spectral effects are consistent with the signature of npFe present in the weathered rims of the top-most surfaces of lunar grains. Ultraviolet observations may not be as strongly affected by large npFe as other spectral regions, because larger npFe particles are typically found within the volume of agglutinates

rather than on the surfaces of grains. This differential sensitivity is consistent with regolith reaching "full maturity" when observed in the UV at somewhat lower values of Is/FeO.

Table 1. Estimated sensing depths ($L = \lambda / 4\pi k$, where λ is wavelength and k is average lunar absorption coefficient) for different spectral regimes.

Instrument	Wavelength, λ	Approx. k	Approx. L
LAMP	160 nm	2.7	5 nm
LAMP	190 nm	0.5	30 nm
LROC WAC	321 nm	0.4	60 nm
LROC, M^3	700 nm	6×10^{-4}	90 µm
M^3	3 µm	1×10^{-3}	200 µm
Diviner	8 µm	0.05	>100 µm
Diviner	10–25 µm	0.5–5	<10s of µm

At visible and near-infrared wavelengths, sensing depths are on the order of tens of nanometers to ~200 micrometers, so typically several to tens of grain depths into the regolith. In this region, the effects of npFe are apparent and can be separated from composition. Comparisons of spectra of sieved and bulk Apollo regolith samples, however, show that particles <25 µm in size, the so-called "finest fraction", show spectral properties most similar to the bulk regolith, and that nanophase iron is still the dominant effect in this spectral region (Pieters et al. 1993; Taylor et al. 2001, 2010). This is because the surface area-to-volume ratio is substantially higher for these small grains, and they thus have a comparatively larger weathered surface; in addition, the finest grains typically cling to and coat larger grains.

In the thermal infrared, at wavelengths well beyond the electronic absorptions of iron-bearing minerals that dominate the visible and near-infrared, spectral variations are driven by a combination of compositional and thermophysical processes. Here albedo differences in the top hundreds of micrometers (tens of grains) of the surface dominate and cause the thermal gradient in the top millimeter to be steeper or shallower, which alters the wavelength position of the Christiansen Feature. The overall lowering of reflectance that occurs due to space weathering is thus the driver of changes to CF position, suggesting the low-reflectance microphase iron within agglutinates may be particularly important for space weathering in the thermal infrared. Unlike the visible and near-infrared, however, the albedo-driven space weathering effect observed in the thermal infrared is not currently separable from the regolith composition (Lucey et al. 2017). Even so, the differences in CF shift observed for highland and mare surfaces suggest an additional, composition-independent maturity constraint may be possible.

With an understanding of the physical ways in which photons in each spectral regime interact with the lunar surface and are differently affected by the changes that occur in that surface as space weathering proceeds, we now have an opportunity to refine our knowledge of the details of these complicated processes that lead to maturity.

3.2 Special lunar environments

Lunar environments with conditions that differ from those of the typical lunar space weathering environment can provide new insights into how space weathering processes operate overall. As the last decade has shown, defining what is "typical" for space weathering is becoming more difficult, as differences in maturity are found not only in distinct areas like magnetic anomalies or permanently shadowed polar regions, but may also vary both latitudinally and longitudinally.

3.2.1 Varying latitudes and longitudes. The angle between the ecliptic plane and the lunar spin axis is only 1.5 degrees, and thus seasonal effects are limited on the Moon. If space weathering agents such as the solar wind have fluxes that are dominantly within the ecliptic, the curvature of the Moon will serve to reduce their effective fluxes at high lunar latitudes (flux will scale with the cosine of latitude). Hence, the lunar surface may be less mature with increasing distance from the equator and recent work has examined this hypothesis.

Maps of global reflectance from the SELENE Spectral Profiler have demonstrated that latitudes poleward of ~75° have higher reflectance and shallower continuum slopes (i.e. less reddening) (Yokota et al. 2011) (Fig. 12); increasing reflectance at the highest latitudes was also found in LOLA 1064 nm reflectance measurements (Lucey et al. 2014; Lemelin et al. 2016b; Fisher et al. 2017). Even at latitudes below 60°, there appear to be differences in reflectance in the maria that are related to latitude. Hemingway et al. (2015) argued that because the solar wind flux is reduced at lunar swirls (Section 3.2.3), the optical properties observed at swirls and at high latitudes should be similar if their cause is the same. Using a spectral parameter derived from 750 nm and 950 nm reflectance variations observed at lunar swirls (Blewett et al. 2011; Garrick-Bethell et al. 2011), the maturity trends in the maria were indeed found to vary with latitude, when grouped by composition (Hemingway et al. 2015; Fig. 13). Since crustal magnetic anomalies do not impede micrometeoroids, the similarity of the spectral trends at swirls and with latitude suggests that variation in solar wind fluence alone is the cause of latitudinal differences in maturity. Between latitudes of ~75° S and 75° N, the highlands show minimal evidence for variation in this same spectral parameter (Hemingway et al. 2015), and no clear variation in albedo with latitude (Lemelin et al. 2016b). This difference between the spectral behavior of the mare and highlands may be due to the lower FeO content of the highlands (Lemelin et al. 2016b).

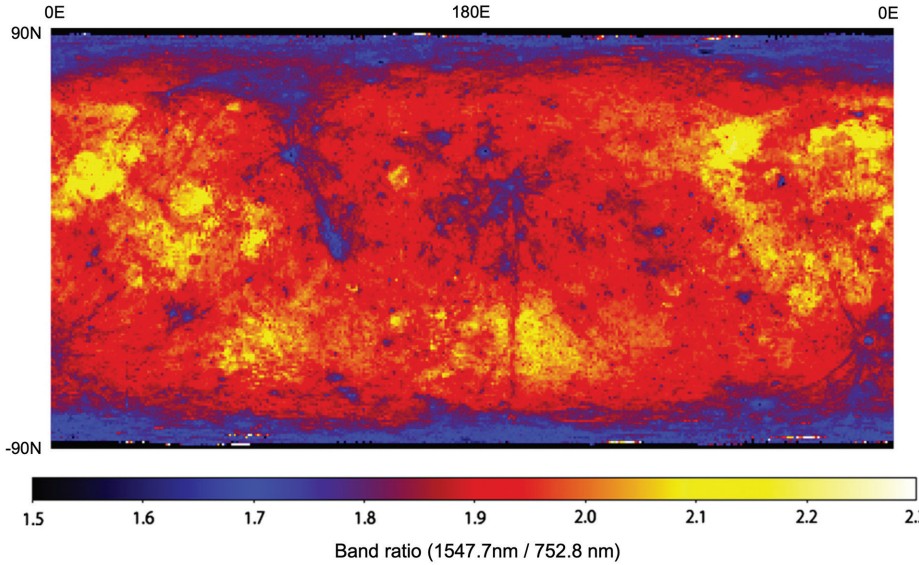

Figure 12. Global map of the 1547.7/752.8 nm ratio from photometrically corrected Spectral Profiler data. The lower ratio values near the poles (corresponding to shallower spectral slopes) have been interpreted as a lower degree of space weathering due to the lower flux of solar wind in those regions. From Yokota et al. (2011).

A similar effect has also been observed in a study of crater walls, which revealed latitude-dependent differences in reflectance that correspond to either the decreased (pole-facing) or increased (equator-facing) flux of the solar wind (Sim et al. 2017). Remarkably, longitude-

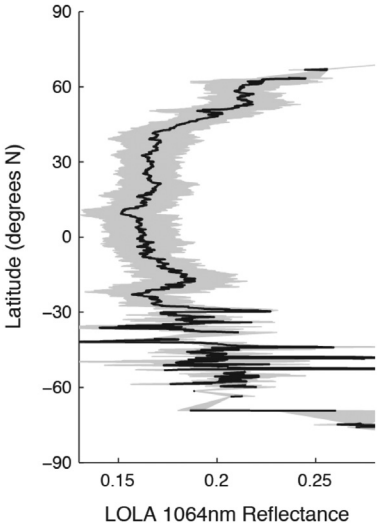

Figure 13. LOLA 1064 nm reflectance for the lunar maria vs. latitude. The reflectance is lowest near the equator and generally higher with increasing latitude (where the solar wind flux is lower), a pattern that holds when the maria are further subdivided by composition. After Hemingway et al. (2015).

dependent reflectance changes on crater walls are also observed. Similar to the differences in solar wind flux that occur with latitude, the passage of the Moon through the Earth's magnetotail each month results in differences in solar wind flux with longitude (Hurley and Farrell 2013). When the Moon is full, it is fully within the magnetotail and almost completely shielded from the solar wind. When local topography is considered, the monthly average solar wind flux on nearside crater walls facing the sub-Earth meridian (0° longitude) is reduced compared to their anti-meridian facing counterparts, with the effect becoming maximal at ±60° longitude (Sim et al. 2017) (Fig. 14). The differences in the reflectance of east-facing and west-facing crater walls mirror these longitudinal differences in solar wind flux (Sim et al. 2017).

Together, these results imply that the flux of the solar wind is important in determining reflectance of a mature regolith (Hemingway et al. 2015; Sim et al. 2017). Because it is thought that the spectral effects of space weathering saturate at the grain level (Hapke 2001), this may imply that there is a relationship between the rate of solar wind-related weathering and regolith gardening, which can expose immature material from depth (see Section 5.1).

Changes in the micrometeoroid flux are also important for optical maturity. Owing to the combination of the motion of the Earth–Moon system revolving around the Sun and the motion of the Moon in orbit around the Earth, the relative velocity between the Moon and the micrometeoroids varies as a function of lunar phase. At full Moon, the velocities are in the same direction, increasing the total relative velocity between the Moon and the population of meteoroids coming from the apex direction. At new Moon, the orbital motion of the Moon is in the opposite direction and reduces the relative velocity of the micrometeoroids. Lunar Dust EXperiment (LDEX) data reveal a phase effect on the amount of dust (ejecta) in the lunar exosphere (Szalay and Horányi 2015). Further comparisons of the variations in micrometeoroid and solar wind flux across the lunar surface (Fig. 15) with observed local spectral properties may prove fruitful.

Finally, recent work has suggested an additional latitude-dependent process may be at work that could result in spectral effects similar to those of other space weathering processes. This process is known as dielectric breakdown, whereby the top ~1 mm of regolith is charged by solar energetic particles to the point of forming electrically conductive channels of vaporized material that dissipate the charge. For dielectric breakdown to occur, the electrically

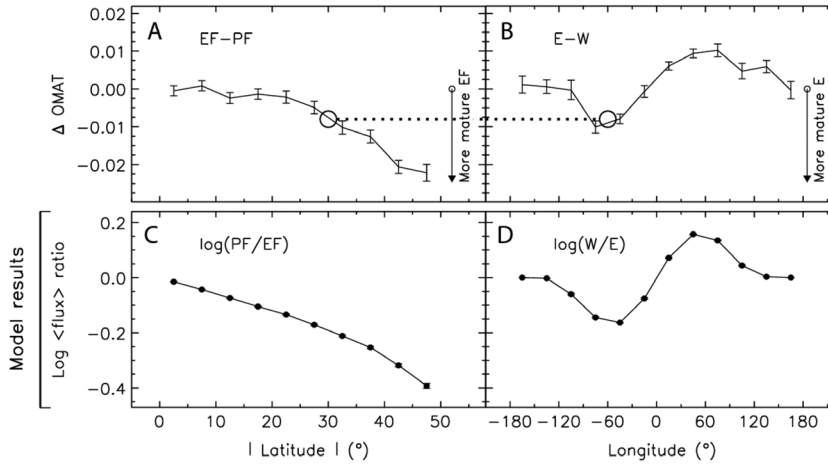

Figure 14. Mean values of OMAT spectral parameter differences between equator-facing (EF) and pole-facing (PF) walls and eastern (E) and western (W) walls are shown in panels **A)** and **B)**, respectively. Data points are the means of all craters in the corresponding latitude or longitude bin, and the error bars are the 1 σ uncertainties of the means. The **arrows** indicate the direction of maturity. Ratios of the mean solar wind fluxes on EF and PF walls are shown in **C)** and E and W walls are shown in **D)**, calculated for craters with the solar wind weathering model described Sim et al. (2017). **Black circles and** lines in panels A and B show that when the solar wind flux is reduced by a factor of 1.5, OMAT difference is reduced by 0.008 for both the E–W and EF–PF effects. More mature surfaces are associated with lower OMAT values. From Sim et al. (2017).

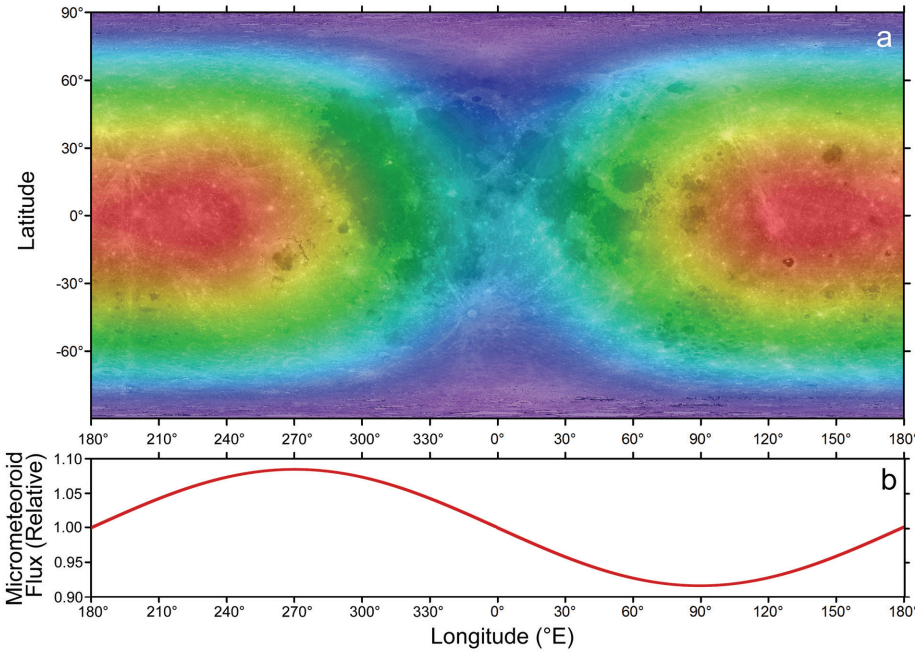

Figure 15. a) The variation of solar wind flux across the lunar surface when thermal effects and the influence of the Earth's magnetotail are considered Hurley and Farrell (2013). Solar wind flux varies by over a factor of five, from ~0.02 (**dark blue**) to >0.10 (**red**) monolayers/lunation. b) Relative micrometeoroid flux as a function of longitude calculated from LADEE LDEX data Szalay and Horáni (2015). Each assumes a spherical Moon with no consideration of local topography.

insulating surface must be charged with fluences exceeding 10^{10} particles cm^{-2} (Feynman et al. 1990). Due to the inverse relationship between discharging timescale and both conductivity and surface temperature, colder surfaces are more likely to acquire sufficient fluence before warming and discharging. Vast areas on the lunar nightside experience temperatures < 100 K (Williams et al. 2017), which corresponds to a discharging timescale longer than ~3 days (Jordan et al. 2017a), on par with the typical length of SEP events. Jordan et al. (2017a) estimated that dielectric breakdown can occur at any latitude, with stronger effects towards the poles (6–12% regolith melted or vaporized) than the equator (2–5% melted or vaporized). This trend, with a larger effect at higher latitudes, would run counter to that of the solar wind, but there has not yet been sufficient observational support for the occurrence of dielectric breakdown on the Moon. Hapke (2022) argues against this process, suggesting that when secondary electron emission and other characteristics of the regolith are taken into account, electric fields sufficient to initiate breakdown are unlikely to occur.

3.2.2 Permanently shadowed regions. Permanently shadowed regions (PSRs) receive no direct solar illumination owing to the combination of topography and the obliquity of the Moon, and thus are a special case for latitude-dependent space weathering. Photons travel in straight lines from the Sun radially outward, and are blocked by high topographic features. The solar wind also travels roughly radially away from the Sun with two important caveats. Because the solar wind speed ($>3\times10^5$ m/s) is 3 orders of magnitude slower than the speed of light (3×10^8 m/s) and only an order of magnitude faster than the speed of the Earth–Moon system in its orbit around the Sun, there is an aberration in the apparent solar wind direction when viewed from the Earth–Moon system that is offset about 3–5° from the subsolar point. Secondly, and more importantly for the PSRs, the motion of charged particles deviates from a straight line owing to the presence of additional forces from electric and magnetic fields. In the frame of reference of a stationary observer, charged particles in the solar wind are convecting with the radial outflow of the solar wind while simultaneously gyrating around magnetic field lines entrained in the solar wind flow. The size and frequency of the gyration relates to the thermal velocity of the particles in the rest frame of the solar wind. This gyration provides some off-axis motion that can begin to fill in the wake region behind a topographic barrier (Halekas et al. 2005; Nishino et al. 2009). Moreover, the electrons in the flow have a higher thermal velocity than their much heavier ion counterparts. Thus, electrons more quickly fill in a wake, effectively separating negative and positive charge in the flow, which establishes an electric field. The electric field attracts the ions into the wake, increasing the rate at which it is filled (Zimmerman et al. 2012; Fig. 16). Through this mechanism, it is expected that solar wind particles have some access to surfaces in PSRs that are (by definition) not accessible to light. Furthermore, there is an anisotropic distribution of the electron flux and ion flux within PSRs such that sputtering occurs from the poleward side.

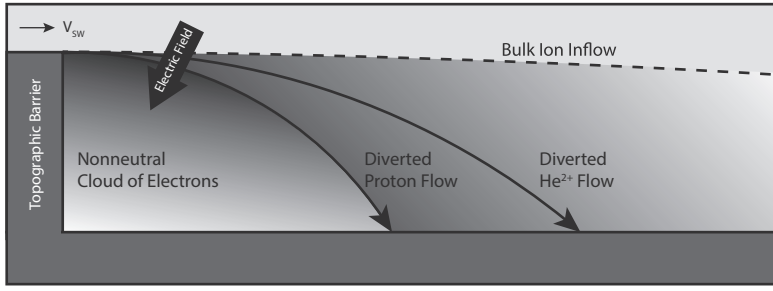

Figure 16. Illustration of how the solar wind can access permanently shadowed regions at the poles. The electrons are less massive and therefore more mobile, which allows them to more rapidly fill the wake behind a topographic barrier, such as a crater wall. This establishes an electric field, which attracts ions into the PSR. After Zimmerman et al. (2012).

This also creates a unique electrical environment. Whereas on the dayside of the Moon, the photoelectric effect kicks electrons off of the surface and produces a positively charged surface, in PSRs the surfaces closest to the obstructed flow charge negatively. If electrostatic forces play a role in regolith grain interactions, such as by producing levitated dust or the large porosity values of the uppermost surface, these processes will be modified in PSRs.

Micrometeoroids do have access to lunar polar regions, including PSRs. Therefore, PSRs will have space weathering caused by micrometeoroids. Because much of the meteoroidal material travels in the ecliptic plane, the flux incident on the poles is reduced by the cosine of the angle between the surface normal and velocity vector compared to lower latitudes. Similarly, the relative velocity for some meteoroids into the PSRs is lower than the equatorial impacts, especially those from the apex direction, because the motion of the Moon has very little component in the z direction. However, micrometeoroids derived from Halley-type (long period) comets and Oort cloud comets have nearly isotropic distributions and can impact the Moon, including polar regions at velocities up to 35 km/hr (Pokorny et al. 2014). Nonetheless, there is a finite flux of meteoroids into PSRs. Whereas magnetic anomalies may represent an environment where micrometeoroids impact regolith with lesser amounts of pre-implanted solar-wind hydrogen, it is not clear whether there is abundant implanted hydrogen in PSRs. There are likely areas with low abundance of solar-wind hydrogen immediately behind obstructing topography. Similarly, the nature of micrometeoroid weathering may be altered in PSRs by the low temperatures, which may decrease the volume of impact melt and vapor, and thus npFe, produced by micrometeoroid impacts (Corley et al. 2016, 2017b). The presence of water ice at quantities of 1–2 wt% (e.g., Gladstone et al. 2012) could also affect weathering if the regolith in PSRs exists as ice-coated grains (Heldmann et al. 2015) and micrometeoroid impacts interact more with the ice coatings than with the underlying grains. This is a topic for further investigation.

Remote sensing observations of the effects of space weathering are, naturally, limited in PSRs. LOLA reflectance data show the albedo within PSRs is ~10% higher than non-PSR polar regions, which could be due to a lower degree of space weathering (Section 3.2.1), and/or the presence of surface frost (Lucey et al. 2014). Comparisons between PSR reflectance and temperature find elevated reflectance in south polar PSRs at the temperatures at which some volatiles are stable, suggesting that surface frost at least contributes to the higher PSR albedo in the south; however, a general inverse correlation between reflectance and temperature (and thus solar wind flux) has been attributed to solar-wind dependent space weathering (Fisher et al. 2017).

While the flux of solar wind and micrometeoroids in PSRs is lower than elsewhere on the Moon, dielectric breakdown may be more important in these locations. Due to the extremely low temperatures (Paige et al. 2010a), the discharging timescale is on the order of weeks, much longer than the typical ~3-day SEP event. Jordan et al. (2017b) estimated that 10–25% of PSR regolith is melted or vaporized via dielectric breakdown, comparable to weathering by meteoroid impacts (Jordan et al. 2013). However, the elevated albedos in PSRs suggest that if dielectric breakdown contributes to space weathering, it may not have a substantial effect on albedo.

3.2.3 Lunar swirls. The albedo features known as lunar swirls may also represent a special space weathering environment, and provide insight into the processes that mature the lunar regolith. Swirls are high reflectance, curvilinear surface features (Fig. 17) that are found in discrete locations across the Moon's surface (e.g., El-Baz 1972; Hood and Schubert 1980; Schultz and Srnka 1980; Denevi et al. 2016), always coincident with magnetic anomalies, although not every magnetic anomaly has an identifiable swirl (e.g., Hood and Williams 1989; Blewett et al. 2011; Denevi et al. 2016). Swirls on the maria are characterized by strong albedo contrasts and complex, sinuous morphology, whereas those on highland terrain often exhibit simpler shapes such as single loops or diffuse bright spots and can be more difficult to discern due to the higher overall reflectance of the highlands and more uneven local terrain. Recent modeling demonstrates the shapes of the swirls are consistent with a surface bisecting various orientations of magnetic field lines (Hemingway and Garrick-Bethell 2012; Poppe et al. 2016).

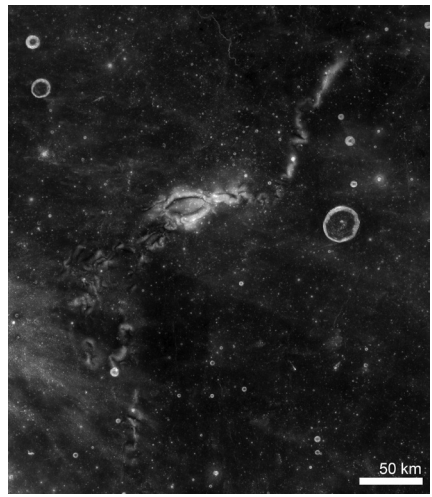

Figure 17. The type example of a lunar swirl, Reiner Gamma, located in Oceanus Procellarum at 7.3°N, 301.0°E. Reiner Gamma includes the high-reflectance, tadpole-shaped feature at center, as well as smaller meandering high-reflectance features that extend to the northeast and southwest. Reiner Gamma may represent either a region of the Moon with anomalous space weathering due to the local magnetic anomaly, a surface that has recently been disturbed to expose immature material, or areas where dust transport has been affected by the local magnetic and electric fields. LROC WAC mosaic at 643 nm.

Multi-wavelength (UV through radar) analyses of swirls have identified a group of spectral characteristics unique to swirls with which any proposed formation mechanism must be consistent. The swirls appear higher in reflectance than their surroundings in UV and VNIR wavelengths, regardless of the illumination geometry. Spectra of the swirls have characteristics (e.g., strong UV absorption, shallower spectral slope, higher OMAT, CF positions at longer wavelengths) suggesting that the degree of space weathering is lower and/or that space weathering operates in an atypical manner in these localized environments (Blewett et al. 2011; Kramer et al. 2011a,b; Glotch et al. 2015; Denevi et al. 2016; Hendrix et al. 2016). Swirls do, however, display spectral differences in comparison to the ejecta of Copernican craters (Hemingway et al. 2015; Pieters and Noble 2016). Whereas fresh impact ejecta have strong absorption bands, the pyroxene crystal field absorption bands of swirls are weaker and show little difference compared to their immediate surroundings. In addition swirls are higher in reflectance across the full VNIR spectrum (Pieters and Noble 2016; Fig. 18). The photometric properties of swirls also indicate that swirls are less backscattering than immature crater ejecta (Schultz and Srnka 1980; Pinet et al. 2000; Kreslavsky and Shkuratov 2003; Kaydash et al. 2009; Kinczyk et al. 2016). The swirls are not associated with a particular terrain type (Bell and Hawke 1987; Pinet et al. 2000; Blewett et al. 2007), nor do they have any topographic, radar backscatter, or thermal structure differences compared to surrounding terrain that would suggest they are anything other than surficial features (Neish et al. 2011; Glotch et al. 2015). The swirls have shallower 2.8 μm absorption bands, indicating they are depleted in hydroxyl and/or water relative to their immediate surroundings (Kramer et al. 2011a; Bandfield et al. 2018).

There are three general classes of hypotheses for swirl formation: (1) recent impacts by swarms of micrometeoroids or cometary coma gas and dust resulting in entrainment of the fine regolith fraction and exposure of unweathered material at the surface (Schultz and Srnka 1980; Bruck Syal and Schultz 2015); (2) deflection of solar wind protons by isolated magnetic fields, resulting in slower or atypical space weathering (Hood and Schubert 1980; Hood and Williams 1989); and (3) electrostatic transport and sorting of regolith based on its size and composition (Garrick-Bethell et al. 2011) or magnetic properties (Pieters et al. 2014).

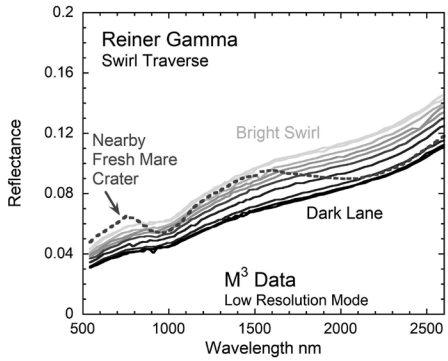

Figure 18. M^3 spectra traversing from a dark lane into a bright swirl in Reiner Gamma. The bright swirl areas exhibit distinct properties compared to immature (unweathered) soils such as found at typical mare craters (see for comparison Fig. 1.4 above) (modified from Pieters and Noble 2016).

The crustal magnetic anomalies have been shown to produce mini-magnetospheres that deflect some portion of the solar wind protons (Futaana et al. 2003; Halekas et al. 2008; Saito et al. 2008, 2012; Lue et al. 2011), though the fraction or energy spectrum of ions that reach the surface is not yet known. Additionally, local suppressions of backscattered energetic neutral atoms have been observed at magnetic anomalies, consistent with a lower degree of sputtering of these atoms by the solar wind (e.g., Wieser et al. 2010; Vorburger et al. 2012; Futaana et al. 2013). The spectral characteristics of swirls are consistent with a lower degree of space weathering or an altered space weathering process (Blewett et al. 2011; Kramer et al. 2011a,b, Glotch et al. 2015; Denevi et al. 2016; Hendrix et al. 2016), which could result from this decreased solar wind fluence and would imply that micrometeoroid bombardment contributes less significantly to space weathering. However, laboratory experiments simulating micrometeoroid bombardment (Section 4.1) and observations of micro-craters (Section 2.2) demonstrate that micrometeoroid impacts can result in substantial optical maturation through production of npFe without charged particle irradiation. The UV spectral characteristics of the swirls are consistent with a less mature surface, but could equally indicate a higher abundance of impact glass that lacks high abundances of larger npFe inclusions (i.e., a difference in the agglutinate fraction of the regolith); such a scenario could indicate that production of npFe within agglutinates is aided by the presence of implanted solar wind (Denevi et al. 2016, see Section 5.2.1).

Both the comet impact and electrostatic transport hypotheses incorporate fine fraction entrainment and transport mechanisms to explain the sinuous high albedo swirl markings. These hypotheses are supported by the observation that swirl surfaces are spectrally distinct from immature regolith surfaces (Garrick-Bethell et al. 2011; Pieters and Noble 2016) and photometric measurements that could suggest alteration of the regolith surface structure (Schultz and Srnka 1980; Pinet et al. 2000; Kreslavsky and Shkuratov 2003; Kaydash et al. 2009). However, thermal infrared observations indicate that neither the thermal structure nor roughness at the millimeter–centimeter scale of the swirls differs from that of the surrounding terrain (Glotch et al. 2015), suggesting that the observed spectral differences are not attributable to the physical state of the swirl regolith on those spatial scales. Determining the cause of the anomalous spectral properties at swirls could provide insight into the overall relationship between space weathering processes and surface maturity in different environments.

4. LABORATORY ANALOG STUDIES

Simulating the processes and effects of space weathering in the laboratory has proved challenging, but much progress has been made in the last decade. Although no single study is able to capture all the elements of space weathering under laboratory conditions and timescales, different approaches have allowed for specific components of weathering to be examined and better understood.

4.1 Micrometeoroid bombardment simulation—laser studies

Pulsed laser irradiation experiments are intended to replicate the physical, chemical, and optical changes produced by hypervelocity impacts of micrometeoroid particles into the surfaces of airless bodies. Lasers with pulse durations of a few nanoseconds (i.e. with energy deposition times that are typical for micrometeoroid impacts) were first suggested as tools to simulate the melting and vaporization that result from dust particle impacts (Kissel and Krueger 1987). Although the first such experiments designed specifically to investigate optical maturation due to micrometeoroid impacts used pulse widths that were approximately three orders of magnitude too long, they did show that physical and spectral changes occur as a result of laser irradiation (Moroz et al. 1996), and additionally confirmed that npFe formation does not require a reducing environment. Subsequent laser weathering studies used shorter pulse lengths (<10 ns) and found a reduction of albedo and substantial reddening, but decreases in 1- and 2-μm absorption band depths were not as significant as in mature regolith (Yamada et al. 1999). Laser irradiation has also been shown to result in a greater reduction of albedo and degree of reddening for olivine relative to pyroxene (Yamada et al. 1999), consistent with remote observations of surfaces of varying composition (Staid and Pieters 2000; Nettles et al. 2011), with potentially important implications for differential space weathering (Lucey 2004; Crites and Lucey 2015; Gross et al. 2015).

TEM and electron spin resonance (ESR) observations of laser-irradiated materials confirmed that the optical changes resulted from vapor-generated npFe (Sasaki et al. 2001, 2003). Successive laser irradiation has also reproduced the progression of weathering observed on the lunar surface, where reddening precedes substantial darkening (Loeffler et al. 2016). TEM observations of materials showed that even after the continuum stopped reddening, npFe continued to form with additional laser irradiation. The successive laser pulses created new npFe particles while simultaneously combining small npFe into larger "microphase" iron, which acted to decrease the albedo. These results suggest that the larger size distribution of iron particles in agglutinates may be due to successive remelting and the coalescence of smaller particles.

The most common method of simulating micrometeoroid impacts uses short pulse Nd:YAG (neodymium-doped yttrium aluminum garnet) lasers with a fundamental wavelength of 1064 nm (e.g., Yamada et al. 1999; Kurahashi et al. 2002; Sasaki et al. 2003; Noble et al. 2011), though UV excimer lasers (Brunetto et al. 2006), visible wavelength lasers (Wu et al. 2017), and femtosecond lasers (Fazio et al. 2018) have also been used. Other techniques have successfully simulated npFe production by using a two-step thermal treatment of olivine grains (Tang et al. 2012; Kohout et al. 2014), microwave heating (Tang et al. 2012), in situ heating in the TEM (Thompson et al. 2017), or magnetron sputtering on lunar simulant grains (Tang et al. 2012; Kohout et al. 2014).

Comparisons of spectral trends observed for lunar samples of varying maturity and for materials weathered experimentally indicate that reproducibility of lunar regolith maturity trends varied by method (Kaluna and Gillis-Davis 2017). Similarly, the validity of equating energy deposited through laboratory laser irradiation to the energy deposited through micrometeoroid impacts that include substantial shock effects is unclear. Hence, not only the process being simulated but the experimental setup itself must be evaluated to validate that the experiment faithfully reproduces the mechanisms acting on the lunar surface.

4.2 Laboratory impact studies

Laboratory experimental impact techniques based on either flat-plate accelerator (FPA) shock recovery experiments, or use of a chemical/light gas gun (LGG) projectile accelerator, have both yielded results relevant to lunar space weathering. Because they employ mm-size projectiles fired in vacuum to hit a solid rock or granular powder target, LGG experiments have the highest degree of fidelity to natural small-scale impacts occurring on the lunar surface. A

key limitation, however, is that LGG projectile velocities are restricted to <6 km/s in routine use, with limited-used extension up to ~7.5 km/s, much lower than the velocities of typical lunar micrometeoroid impacts. Variations in impact velocity are known to have significant effects. For example, LGG experiments have shown that lower impact velocities (0.7–1.4 km/s) are more efficient for rapidly comminuting a starting whole-rock target, but higher velocities (>1.9 km/s) are required to reduce the target to typical lunar regolith grain sizes (Hörz et al. 1984; Cintala and Hörz 1988; See and Hörz 1988). LGG experiments performed at 5.4–5.5 km/s into granular gabbro and artificial highland regolith targets produced significant shock melting and formed melt-welded grain aggregates with a strong morphological resemblance to lunar agglutinates (See and Hörz 1988; Corley et al. 2017a). However, TEM analyses of these products failed to find any npFe or other metallic particles in the glass that were not derived from the metallic impactor (Christoffersen et al. 2013) and the measured reflectance spectrum of the agglutinates did not show any appreciable difference from that of the target material (Corley et al. 2017a).

Currently, the restriction of FPA and LGG impact techniques to projectile speeds and/or shock stresses corresponding to impact velocities generally less than 7 km/s prevents these experiments from fully exploring the effects produced across the entire velocity distribution of micrometeoroids striking the lunar surface. This includes impacts occurring at the postulated lunar mean impact velocity of ~12 km/s (Hartmann 1977; Bottke et al. 1994). From the experiments so far, it appears that impacts into lunar-composition targets at velocities as low as 4–5 km/s are above the threshold for producing significant shock melting and agglutinate formation. However, the laboratory agglutinates are not optically dark, because they lack npFe inclusions (Christoffersen et al. 2013; Corley et al. 2017a). Although it is easy to hypothesize that npFe formation in the laboratory simply requires higher impact speeds, this will not be confirmed experimentally until the required kinetic conditions can be achieved. An alternative kinetic impact experimental approach that has some potential in this regard is the use of Van de Graff-type electrostatic dust particle accelerators to investigate small-scale impact effects at the required higher velocities (e.g., Shu et al. 2012). Although not widely applied to space weathering problems as yet, preliminary results from experiments relevant to space weathering are starting to appear (Christoffersen et al. 2017; Fiege et al. 2019).

4.3 Solar wind simulation—ion irradiation studies

The predominant components of the solar wind (H^+ and He^+ ions with total energies in the range of 1–5 keV) can be duplicated using various ion gun and vacuum chamber arrangements in the laboratory (Johnson 1990). The solar wind ion irradiation processes of interest for study in the laboratory include changes induced by both direct irradiation and indirect effects. Simulated direct irradiation effects include disruption and possible eventual amorphization of crystal structures (ion damage), and one of the key drivers for performing ion irradiation experiments is to calibrate the critical amorphization fluence for the dominant solar wind ions. Because the collisional damage efficiency of all ions declines as they enter a target crystal and slow down, damage leading to amorphization can be expected to vary with depth, becoming deeper with increasing fluence (but still limited by the range of penetration of the ions involved). If the ion flux is known, the growth can be calibrated with respect to irradiation time. These relations have formed the basis for quantitative models that endeavor to link the thickness of solar-wind amorphized rims on space weathered grains to their integrated direct solar wind exposure time (e.g., Chamberlin et al. 2008; Christoffersen and Keller 2015; Poppe et al. 2018; Keller et al. 2021).

To date, the principal lunar minerals plagioclase, pyroxene, ilmenite and olivine have all been the subject of laboratory ion-irradiation studies supported by TEM imaging (e.g., Carrez et al. 2002; Christoffersen et al. 2010a; Kuhlman et al. 2015). These studies have varied in their objectives, as well as the fidelity of their conditions to solar wind conditions (ion species and energy) and the end fluences attained. A common approach of these studies is to use high fluences (10^{17}–10^{18} ions/cm^2) that achieve demonstrable damage, to simulate solar system

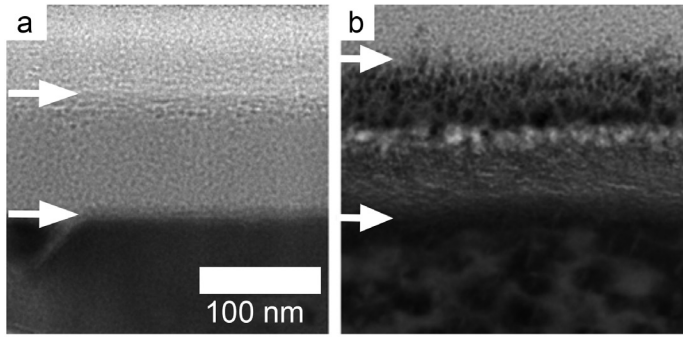

Figure 19. Transmission electron microscope images of the upper 400 nm of plagioclase **(a)** and ilmenite **(b)** single crystals prepared by focused ion beam (FIB) cross sectioning after they were ion irradiated in the laboratory with 4 keV He^+ ions and coated with amorphous carbon. **(a)** Is a conventional bright-field TEM image of an An_{90} lunar plagioclase prepared from an interior thin section of lunar basalt 70035 and ion irradiated to a final He^+ fluence of 1.2×10^{17} ions/cm^2, **(b)** is a bright-field STEM image of a synthetic ilmenite ($FeTiO_3$) grain ion irradiated to a final He^+ fluence of 3×10^{17} ions/cm^2. **Arrows** show the upper and lower boundary of the ion damaged layer in each sample, which in plagioclase **(a)** is uniformly amorphous with a thin implantation bubble layer at the top. The ilmenite **(b)** shows three distinct nano-crystalline/partially ion damaged layers, including an uppermost layer containing abundant nanophase Fe^0.

processes on laboratory timescales (e.g., Carrez et al. 2002). Figure 19 shows TEM images of two such high-fluence samples: plagioclase and ilmenite single crystals both experimentally ion irradiated with 4 keV He^+ to fluences in the 10^{17} range (Christoffersen et al. 2010a). The strong contrast in ion processing behavior of the two materials exemplifies the key role of composition and intrinsic crystal chemistry in determining how minerals respond to solar wind exposure.

In addition to structural damage, laboratory simulations have demonstrated that the direct effects of ion irradiation at typical solar wind energies also include the inducement of compositional changes, including the segregation of cations and depletion of oxygen, in the outer 5–10 nm of a crystal due to preferential sputtering erosion (Loeffler et al. 2017). In the absence of assistive processes, such as heating and diffusion, preferential sputtering is incapable of producing chemical changes that penetrate more than a few nm below the surface of a crystal. In some natural lunar minerals such as ilmenite, however, chemical changes can extend much deeper (20–30 nm), suggesting additional chemically active ion irradiation processes and/or thermal effects are required, though they remain poorly understood (Christoffersen et al. 1996; Zhang and Keller 2010; Burgess and Stroud 2018; Laczniak et al. 2021).

As part of his space weathering overview, Hapke (2001) reviewed experimental evidence suggesting that direct ion irradiation was relatively ineffective in altering the optical reflectance properties of lunar analog minerals. More recently, however, Loeffler et al. (2009) showed that, at least for olivine, surface formation of npFe driven by preferential sputtering during direct He^+ ion irradiation can produce reflectance changes significant for remote sensing. This has revived interest in direct ion irradiation as a way to explain the optical space weathering of S-type asteroids, leaving open the possibility that it may be important on the Moon as well. TEM studies of He^+-irradiated ilmenite and pyroxene have also shown surface-correlated npFe formation similar to that in olivine, further suggesting that optical effects from direct solar-wind irradiation may play a role in lunar optical space weathering (Christoffersen et al. 2010a,b).

Laboratory experiments have also attempted to simulate the indirect effects of solar wind radiation: surface deposition of species that solar-wind ions have sputtered from surrounding areas of the regolith (generally at the cm scale). A variety of experiments have shown that progressive H^+ irradiation causes porous materials to darken, possibly due to deposition of

optically dark sputter deposits on grain surfaces shielded from the direct ion beam (see Hapke 2001). These experimental findings have supported the idea that sputter deposition may be responsible for, or contribute to, the optically dark npFe-bearing grain rim deposits described by Keller and McKay (1993, 1997). The pattern of volatile element enrichments in Si, Fe and especially S in natural lunar grain rims has led to the suggestion that these rims are dominated by impact vapor deposits, as opposed to sputter deposits (Keller and McKay 1993, 1997), and some evidence that sputtering induces little elemental fractionation in lunar composition materials has been reported (Christoffersen et al. 2012). However, better data on the compositional signatures of sputter deposits produced under solar wind relevant experimental conditions is needed, and could provide insight into the relative importance of sputter- and vapor-produced deposits. More comprehensive experimental sputtering studies are needed.

5. DISCUSSION

5.1 Current knowledge of space weathering rates

It is of interest to establish the rates at which space-weathering processes operate. For example, given sufficient knowledge about the rate at which optical changes occur, it might be possible to devise a method for determining absolute ages of surfaces based on remote measurements. Information on space-weathering rates comes from sources that include analysis of the spectral characteristics of lunar crater ejecta, observations of the current rate at which small lunar craters are forming in the present day, examination of returned samples, laboratory space weathering simulations, and theoretical considerations. However, integrating these into a coherent story of the rate of maturation of the lunar surface is not straightforward. Remote sensing, laser irradiation/impact experiments, and analysis of returned lunar regolith samples each yield results with potentially very different time perspectives.

Laboratory simulations of various aspects of space weathering have offered insights into rates of space weathering. Hydrogen-ion irradiation of loose silicate powders caused darkening and reddening of the powders that were observed to saturate at ion doses that correspond to about 10^5 years on the Moon (see Hapke 2001). Laser-shot processing, intended to simulate space weathering by micrometeoroid bombardment, has been shown to produce nanophase iron and spectral changes typical of lunar-style space weathering with an energy that corresponds to ~10^8 years of micrometeoroid bombardment at 1 AU (Sasaki et al. 2001).

Analysis of lunar samples has also provided estimates of space weathering rates by examining the microstructural and chemical features in returned samples that are produced by space weathering processes. Based on a new calibration of the rate of production of solar energetic particle tracks in surface-exposed lunar grains, Keller et al. (2021) used TEM measurements of track densities in individual grains to calculate their exposure ages. Correlation of the track-based ages with the microstructure and width of vapor-deposited and solar wind damaged rims on the same grains revealed that the widest ion-damaged rims corresponded to exposure ages in the range of 10^6–10^7 years.

When the spread and mean values of grain exposure ages were correlated with the maturity indices for different regolith samples, Keller et al. (2021) also saw evidence that mature regolith characteristically had average grain ages in the same range of 10^6–10^7 years. This relationship suggests a similar timescale for the gardened upper layers of regolith to become optically mature, and as noted below this value is within an order of magnitude of gardening rates indicated by remote sensing (e.g., Speyerer et al. 2016). This rate is, however, faster than that indicated by remote sensing of the optical maturity (OMAT parameter) of the lunar crater Copernicus (Grier et al. 2001; Hawke et al. 2004). The ejecta of Copernicus is nearly fully mature; with only a slight increase in the degree of weathering, the ejecta of Copernicus

would reach an optical state indistinguishable from that of the mature background regolith. The age of Copernicus has been estimated as 0.8–1.1 × 10^9 years based on radiometric ages of a glassy sample collected at the Apollo 12 site, located along a Copernicus ray. Thus, it could be surmised that it takes ~0.8–1.1 Gy for lunar optical maturity to achieve steady state.

The difference between the sample analysis/laboratory simulations and remote sensing observations can be reconciled by understanding the geologic setting of immature materials. Immature material is typically exposed by impact craters in an ejecta deposit of a thickness that increases with crater size. For small craters, as space weathering progresses, mature regolith is also gardened into the ejecta deposit from beneath the thin ejecta layer. For larger craters, as the surface ejecta matures, gardening can result in the exposure of immature materials from within the ejecta deposit, and the breakdown of rocks produces new immature regolith. Thus, factors related to the size of a crater and its geological setting, including the thickness of the ejecta deposit and the size of ejecta fragments, control the time required for ejecta material to reach maturity (Lucey et al. 2000; Grier et al. 2001; Hawke et al. 2004; Ghent et al. 2014). Differences in these factors also lead to variations in the amount of time required for various portions of a crater (interior vs. proximal ejecta vs. distal ejecta) to reach full optical maturity.

The rate of gardening of a regolith thus also plays a critical role in the rate of maturation of a surface. Observations of hundreds of newly formed impact craters and tens of thousands of changes in surface reflectance, suspected to be largely secondary impacts, demonstrated that the upper ~2 cm of regolith will be gardened in ~10^5 years (Speyerer et al. 2016). This new understanding of the rate of regolith gardening may provide insight into the rates of space weathering on the lunar surface. For example, the observation that areas of lower solar-wind flux appear to reach a lower level of maturity (Section 3.2) rather than simply saturating after a total accumulated solar wind dose, could be explained if solar-wind related optical changes to the regolith occur on a timescale over which regolith gardening can continually expose immature material to the surface. Further comparisons of models of regolith gardening rates with depth (e.g., Costello et al. 2018) and rates of maturation due to the effects of the solar-wind and micrometeoroid bombardment may provide new insights into the interplay between these processes.

5.2 Current understanding of the relative roles of micrometeoroid impacts and solar wind irradiation

The canonical view that micrometeoroid impact and solar wind ion irradiation are the dominant processes that drive lunar space weathering suffers from a major knowledge gap: several important space weathering features, including some with important links to remotely sensed optical reflectance properties, are not fully resolved with respect to being formed by either impact or solar wind ion irradiation processes, or a combination of both. Two of the most important examples discussed below are the formation of npFe grains that reside in both agglutinates and the deposited outer layers on regolith grains.

5.2.1 Formation of nanophase Fe in lunar agglutinates. As outlined in previous sections, agglutinates are produced when micrometeoroids impact into fine-grained regolith target material. What is less well-established, however, is whether the ubiquitous npFe grains found in the shock-melted (now glassy) agglutinate matrix are solely a byproduct of the impact melting and vaporization conditions, or whether their formation during the impact event is somehow assisted by, or even requires, the presence of implanted solar wind H in the target grains. In the latter scenario, first discussed by Housley et al. (1973), H is hypothesized to promote Fe reduction in the melt phase to form the molten metallic Fe droplets that eventually solidify as npFe. The detailed mechanisms may involve reactive combination of H with O to form H_2O which could then escape the melt phase as a volatile species or be retained in the regolith (Liu et al. 2012; Greer et al. 2020).

A countervailing concept to the H reduction hypothesis is that the extreme temperatures attained during shock melting in micrometeoroid impacts under vacuum on the lunar surface may be sufficiently reducing by themselves to form metallic Fe without the need for implanted H (Housley et al. 1973; Hapke 2001). In this case O is simply lost as a volatile species during the impact vaporization processes that accompany impact melting. The chemical transport and reaction conditions under this impact-only scenario are envisioned to be sufficiently rapid at impact temperatures to overcome the very short cooling timescale of the associated shock melt. As noted in Section 4.1 above, abundant npFe is routinely produced in pulsed laser irradiation experiments using starting materials that do not contain implanted or other types of additional H. If the thermal and vaporization conditions in these experiments are indeed analogous to those in micrometeoroid impacts, then this would seem to remove a required role for solar wind H. If the analogy between pulsed laser conditions and those in small-scale micrometeoroid impacts is incomplete, however, a role for implanted solar wind H remains open.

Remote sensing data suggests the solar wind does indeed play a role in altering the spectral properties of the lunar surface, and thus in producing npFe. Much of the last decade's work studying the spectral properties of swirls and space weathering trends on the Moon as a function of latitude and now longitude (Section 3.2) has been interpreted to suggest that the solar wind is a critical weathering agent. This interpretation stems from the observation that areas that are thought to experience a reduced solar-wind flux, but little or no difference in micrometeoroid flux, are high in reflectance and have other spectral characteristics suggesting they are less mature due to slower or anomalous space weathering. However, while swirls (Pieters and Noble 2016) and poleward facing crater walls (Sim et al. 2017) maintain relatively high reflectance values across visible–near-infrared wavelengths, they do show one hallmark of space weathering: reduced mafic absorption band strength (Fig. 20). These remote sensing observations for locations where high-reflectance materials have weakened band depths suggest that micrometeoroid bombardment may play an important role in decreasing absorption band depth, but alone cannot substantially darken materials, and thus the solar wind is required for a general reduction in reflectance. This may suggest that micrometeoroid bombardment alone can indeed produce metallic iron in some abundance, but greater abundances or larger particle sizes require the solar wind, perhaps aiding reduction of Fe as implanted H, if not via sputtering.

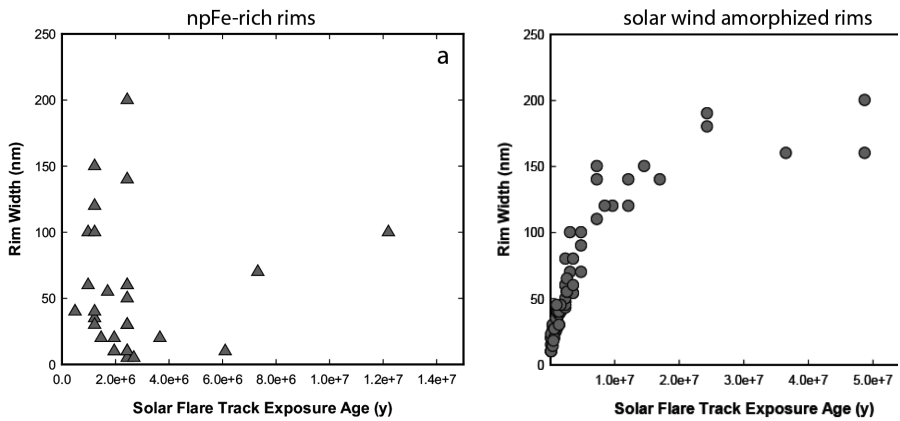

Figure 20. a) Thickness of npFe-rich rims of anorthite grains from several lunar soils with a range of maturity (67701, 10084, and 62231) vs. the exposure age derived from solar flare tracks for each grain. Rim thickness shows no correlation with exposure age. **b)** Solar wind amorphized rims on lunar anorthite grains shows an increase in rim thickness with exposure age until saturation is achieved. After Keller and Zhang (2015).

Additional studies are needed to resolve the issue of npFe formation in agglutinates. Projectile impact experiments into regolith-analog target materials at impact speeds covering the 5–50 km/s range applicable to lunar micrometeoroids would provide a critical test of whether micrometeoroid bombardment alone can produce the npFe in agglutinates. As noted in Section 4.2, impact experiments at the lower range (5–7 km/s) of these speeds did not form npFe in their shocked samples (Christoffersen et al. 2013); neither did electrostatically-accelerated dust particles traveling at 15–18 km/s (Christoffersen et al. 2017). Unfortunately, the highest relevant velocities have not been explored because it is not yet technologically possible to perform impact experiments that achieve these speeds under the required vacuum and other conditions that mimic the lunar surface. In situ investigations of the lunar regolith in regions of varying solar wind flux, such as within a swirl/crustal magnetic anomaly (Blewett et al. 2022) or at near-polar latitudes, will provide new information about how space weathering proceeds in regions where solar wind flux and implanted solar wind abundance may be lower. Returned samples from such locations would enable detailed studies of npFe within agglutinates.

An additional process that has been discussed with regard to npFe in lunar agglutinates is the thermal "recycling" of small metallic Fe grains across multiple micrometeoroid impact cycles. This has been proposed as a mechanism that may allow npFe grains initially formed in the 10–100 nm size range within agglutinate glass to coalescence and coarsen into larger micrometer-scale grains when the glass is re-melted in subsequent impacts. Such effects were observed in lunar samples subjected to repeated thermal events during TEM analyses (Thompson et al. 2017). In addition to thermally processing pre-existing npFe grains in agglutinate material, it is likely that additional new reduced Fe may be generated in the target material in each cycle.

5.2.2 Formation mechanisms of nanoscale deposits on lunar regolith grains. As discussed in Section 2, mechanisms associated with solar wind ion sputtering and/or condensation of impact-generated vapors have both been considered as ways to form the nanoscale outer layers containing npFe that make up part of lunar grain rims. Much of the early work in evaluating these two mechanisms has been summarized by Hapke (2001). This summary includes results from a number of early experiments showing that ion irradiation of Fe-bearing porous mineral aggregates produced optical darkening, which was inferred to be from sputter deposits forming on the undersides of grains. The analogous mechanism in the natural lunar regolith would presumably involve sputter-transfer of material from grains directly exposed to the solar wind to adjacent shielded grain surfaces. Another conceivable, but little discussed possibility is that solar wind sputtering across the larger-scale regolith surface could produce a resident thin exosphere-like vapor cloud whose components re-deposit on exposed grains. For impact vapor deposition, the process is typically envisioned to involve generation of localized high-temperature impact vapor around the site of micrometeoroid impacts with similarly localized recondensation of the vapor on adjacent exposed grain surfaces.

Data and evidence necessary to resolve the relative roles of sputtering or impact vapor deposition in forming npFe on lunar grains come from the observations of the deposits themselves, as well as from relevant experiments, modeling of the two processes, and the examination of remote sensing data. For the deposits themselves a key piece of evidence resides in the major element relative abundances measured in the Keller and McKay (1997) analytical TEM studies. The excellent correlation between the measured relative element abundances and data on their relative volatilities, particularly for elements such as S and Na, is what led Keller and McKay (1997) to favor an impact vapor deposition origin. For sputter deposition to be a similarly viable process, sputtering must generate deposits with a matching pattern of volatile element enrichment. One problem, however, is that the relative abundance of elements derived from multi-component sputtering is primarily a function of sputtering yields, which only partly correlated with volatility but include controls linked to atomic number and surface chemical binding effects (Johnson 1990). Reliable determination of sputtering yields for lunar-relevant

materials are still in the process of being collected (e.g., Meyer et al. 2011), but an early set of empirical sputtering yield data summarized by Hapke (2001) show patterns of element relative depletions and enrichments that do not match the measured deposit compositions. A more recent TEM study of an experimental sputtering deposit produced by sputtering a glass of lunar regolith composition produced a completely amorphous deposit containing no npFe, and which showed no strong pattern of element enrichment/depletion relative to the target material (Christoffersen et al. 2012). It is notable, by comparison, that the several sputtering experiments that produced sample darkening described by Hapke (2001) were only analyzed optically, with no confirmation of the microstructure and chemical composition of the deposits by electron microscopy or other spatially-resolved analytical techniques.

Whereas the weight of current laboratory experimental evidence tends to support the idea that the outer layers of deposited material on lunar regolith grains are most likely condensed impact vapors, further research on sputter deposition under conditions relevant to the lunar regolith surface environment is needed to resolve the question. The Christoffersen et al. (2012) sputter deposition experiments, although generally applicable, nevertheless utilized very high-flux Ga ions that were not an appropriate analog to the solar wind. A similar experimental and sample characterization approach using ions with compositions, fluxes and energies that match the solar wind, would likely be a critical experiment for resolving whether solar wind sputtering is actually a viable process for driving the space weathering of lunar regolith grains.

6. FUTURE ADVANCES IN SPACE WEATHERING

Important advances continue to be made in understanding how the solar wind and the rain of micrometeoroids create a mature regolith, and how physical and chemical changes to the surface affect observations of the Moon from far-ultraviolet through thermal-infrared wavelengths. However, certain issues have proven stubbornly difficult to resolve. Some of the major open topics regarding the mechanisms and rates of space weathering include:

6.1. Solar wind vs. micrometeoroids

Many space weathering studies, whether based primarily on analysis of remote sensing data, laboratory simulations, or examination of samples, focus on understanding the role(s) of the solar wind vs. micrometeoroid bombardment. A fundamental outstanding question is whether, in the aggregate, one process dominates (e.g., results in more rapid changes or changes that have larger spectral effects), or whether both are required to produce a "typical" mature regolith (e.g., solar-wind implantation aids in reduction of iron during micrometeoroid bombardment). Further work is needed to confirm production of npFe with high-velocity impact experiments, to examine the process and products of solar wind sputtering via experiments, and to collect and characterize samples weathered in distinct lunar environments. The balance of evidence from samples, experiments, and remote sensing data is not clearly tipped in either direction, and therefore this is likely to remain an important focus of space weathering research in coming years.

6.2. Lunar swirls

Crustal magnetic anomalies provide some degree of shielding from the solar wind, and host lunar swirls that, by many measures, appear immature. Determining if the lower flux of solar-wind ions is responsible for the presence of swirls could provide another opportunity to gauge the relative importance of solar-wind vs. micrometeoroid bombardment in the maturation process. Alternately, if another process is responsible for their formation, swirls may provide insight into other lunar surface processes. Determining whether one mechanism can explain the anomalous spectral properties from UV through mid-IR wavelengths while leaving the topographic and thermophysical properties unchanged will aid in understanding these features.

6.3. Rates

Improving our understanding of what information laboratory space-weathering experiments provide about rates of maturation is important for advancing our knowledge of lunar space weathering rates. Key questions include: 1) Is it possible to accurately simulate solar-wind irradiation in the laboratory using fluxes much higher than the solar wind? 2) Can the energy deposition from laser experiments easily be translated to micrometeoroid energy deposition amounts and rates? Determining how or if we can translate these laboratory-derived rates into rates of maturation of the lunar surface will also involve an evaluation of rates of gardening with depth and how larger impact events complicate a straight path to maturity by burying and re-exposing regolith. Further work is also needed to explore the timescales for the evolution of microstructural and chemical products of space weathering (e.g., the oxidation of npFe particles)

6.4. Variations across the Solar System

The Moon still provides our baseline knowledge of how space weathering operates. Exploring space weathering in distinct lunar environments (e.g., high latitudes, swirls) may provide new information about how weathering proceeds on airless silicate bodies closer to and farther away from the Sun. Differences in space weathering on other airless bodies may also provide a new framework to understand the relative importance of the range of processes responsible for lunar space weathering.

6.5. Other processes

New work should evaluate what role does dielectric breakdown plays in the maturation of the lunar surface. As we continue to explore the Moon, we may also learn about other processes exist that may have ramifications for space weathering and maturation, that we have, thus far, failed to appreciate.

These topics may be addressed in a variety of ways. High-resolution images from the Lunar Reconnaissance Orbiter Cameras have revealed striking details of fresh impact craters, but many such features are smaller than the scale of a pixel in other multi- and hyperspectral observations; meter-scale multispectral images would provide critical new information. Hyperspectral imaging (from UV through mid-IR wavelengths) of the Moon, begun by the Moon Mineralogy Mapper, and to be extended by Lunar Trailblazer (Ehlmann et al. 2022) should be completed in order to provide a more complete view of maturity differences across the globe.

Also of importance are future in-situ observations and returned samples of mature and immature regolith. The Lunar Vertex investigation at the Reiner Gamma swirl, carrying a suite of imaging, spectral, plasma, and magnetic field sensors, will provide new information to improve our understanding of the relative roles of solar-wind and micrometeoroid bombardment in surface maturation (Blewett et al. 2022). Future returned samples of swirl regolith, in-situ measurements and returned samples of high-latitudes and PSR regolith will also yield insights into how regolith matures in regions with lower solar wind flux.

Ever more realistic laboratory simulations of space weathering will also continue to be fruitful. Low-flux irradiation experiments would more accurately replicate the solar wind at the Moon and may provide a better understanding of the process and rates of maturation of surface materials. Transitioning from nanosecond pulsed laser experiments to femtosecond lasers or dust impact experiments could prove beneficial. It is also critical to confirm that pulsed laser experiments indeed produce faithful analogs to materials impacted by micrometeoroids. Laboratory impact experiments have not yet been shown to produce npFe in target materials. Thus, kinetic impact experiments at higher velocities more representative of lunar impactors, such as those possible with electrostatic dust particle accelerators, could confirm conventional wisdom or provide surprising new results.

Remotely sensed data, particularly for bodies such as Mercury and asteroids, will continue to provide important new information. If we are to expand our knowledge of the myriad of Solar System bodies unlikely to be targeted for sample return, it will also be crucial to perform coordinated TEM, synchrotron X-ray, and UV–mid-IR spectral analyses of the samples of airless bodies that we do have, as well as experimentally weathered samples. Models that enable determination of the degree of space weathering, such as radiative-transfer models of the absorbing and scattering properties of nanophase iron and other opaques, will also need further refinement to ensure they accurately extract information from remote data.

The desired advances in space weathering described here are readily attainable, and require a sustained effort in the laboratory, in remote data collection and analysis, and in advocacy for and development of missions that will make the needed in-situ measurements and return samples.

REFERENCES

Abe M, Takagi Y, Kitazato K, Abe S, Hiroi T, Vilas F, Clark BE, Abell PA, Lederer SM, Jarvis KS, Nimura T (2006) Near-infrared spectral results of asteroid Itokawa from the Hayabusa spacecraft. Science 312:1334–1338

Adams JB, Jones RL (1970) Spectral reflectivity of lunar samples. Science 167:737–739

Anderson BJ, Johnson CL, Korth H, Purucker ME, Winslow RM, Slavin JA, Solomon SC, McNutt RL Jr, Raines JM, Zurbuchen TH (2011) The global magnetic field of Mercury from MESSENGER orbital observations. Science 333:1859–1862

Badyukov DD (2020) Micrometeoroids: The flux on the Moon and a source of volatiles. Solar System Res 54:263–274

Baldwin RB (1949) The Face of the Moon. Univ. of Chicago Press, Chicago

Baldwin RB (1963) The Measure of the Moon. Univ. of Chicago Press, Chicago

Bandfield JL, Poston MJ, Klima RL, Edwards, CS (2018) Widespread distribution of OH/H2O on the lunar surface inferred from spectral data. Nat Geosci 11:173–177

Basu A (2005) Nanophase Fe^0 in lunar soils. J Earth System Sci 114:375–380

Bell JF, Hawke BR (1987) Recent comet impacts on the moon—The evidence from remote-sensing studies. Publ Astron Soc Pacific 99:862

Berger EE, Keller LP (2015) Solar flare track exposure ages in regolith particles: A calibration for transmission electron microscope measurements. Lunar Planet Sci 46:1543

Bibring JP, Langevin Y, Maurette M, Meunier R, Jouffrey B, Jouret C (1974) Ion implantation effects in "cosmic" dust grains. Earth Planet Sci Lett 22:205–214

Blanford GE, Fruland RM, McKay DS, Morrison DA (1974) Lunar surface phenomena-Solar flare track gradients, microcraters, and accretionary particles. Lunar Planet Sci Conf Proc 5:2501–2526

Blewett DT, Hawke BR, Lucey PG (2005) Lunar optical maturity investigations: A possible recent impact crater and a magnetic anomaly. J Geophys Res 110:E04015

Blewett DT, Hawke BR, Richmond NC, Hughes CG (2007) A magnetic anomaly associated with an albedo feature near Airy crater in the lunar nearside highlands. Geophys Res Lett 34:L24206

Blewett DT, Coman EI, Hawke BR, Gillis-Davis JJ, Purucker ME, Hughes CG (2011) Lunar swirls: Examining crustal magnetic anomalies and space weathering trends. J Geophys Res 116:E02002

Blewett DT, Denevi BW, Le Corre L, Reddy V, Schröder SE, Pieters CM, Tosi F, Zambon F, De Sanctis MC, Ammannito E, Roatsch T (2016) Optical space weathering on Vesta: Radiative-transfer models and Dawn observations. Icarus 265:161–174

Blewett DT, Halekas J, Ho GC, Greenhagen BT, Anderson BJ, Vines SK, Regoli L, Jahn JM, Kollmann P, Denevi BW, Meyer HM (2022) Lunar Vertex: PRISM Exploration of Reiner Gamma. Lunar Planet Sci 53:1131

Bottke WF, Nolan MC, Greenberg R, Kolvoord RA (1994) Velocity distributions among colliding asteroids. Icarus 107:255–268

Borg J, Chaumont J, Jouret C, Langevin Y, Maurette M (1980) Solar wind radiation damage in lunar dust grains and the characteristics of the ancient solar wind. *In:* Pepin RO, Eddy JA, Merrill RB (eds) The Ancient Sun: Fossil Record in the Earth, Moon and Meteorites, Pergamon Press, New York p 431–461

Braden SE, Robinson MS (2013) Relative rates of optical maturation of regolith on Mercury and the Moon. J Geophys Res: Planets 118:1903–1914

Braden SE, Stopar JD, Robinson MS, Lawrence SJ, van der Bogert CH, Hiesinger H (2014) Evidence for basaltic volcanism on the Moon within the past 100 million years. Nat Geosci 7:787–791

Britt DT, Pieters CM (1994) Darkening in black and gas-rich ordinary chondrites: The spectral effects of opaque morphology and distribution. Geochim Cosmochim Acta 58:3905–3919

Bruck Syal M, Schultz PH (2015) Cometary impact effects at the Moon: Implications for lunar swirl formation. Icarus 257:194–206
Brunetto R, Romano F, Blanco A, Fonti S, Martino M, Orofino V, Verrienti C (2006) Space weathering of silicates simulated by nanosecond pulse UV excimer laser. Icarus 180:546–554
Burgess KD, Stroud RM (2017) Glassy with a chance of nanophase iron: Space weathering of lunar soil as observed with aberration-corrected scanning transmission electron microscopy. Microsc Today 25:32–39
Burgess KD, Stroud RM (2018) Coordinated nanoscale compositional and oxidation state measurements of lunar space-weathered material. J Geophys Res: Planets 123:2022–2037
Bustin R, Carr RH, Gibson EK, Sommer MA (1986) The hydrogen content of lunar soils. Lunar Planet Sci 17:95–96
Bustin R, Kotra RK, Gibson EK, Nace GA, McKay DS (1984) Hydrogen abundances in lunar soils. Lunar Planet Sci 15:112–113
Cahill JTS, Blewett DT, Nguyen NV, Xu K, Kirillov OA, Lawrence SJ, Denevi BW, and Coman EI (2012) Determination of iron metal optical constants: Implications for ultraviolet, visible, and near-infrared remote sensing of airless bodies. Geophys Res Lett 39:L10204
Cahill JT, Thomson BJ, Patterson GW, Bussey DB, Neish CD, Lopez NR, Turner FS, Aldridge T, McAdam M, Meyer HM, Raney RK (2014) The Miniature Radio Frequency instrument's (Mini-RF) global observations of Earth's Moon. Icarus 243:173–190
Campbell-Brown D (2008) High resolution radiant distribution and orbits of sporadic radar meteoroids. Icarus 196:144–163
Carrez P, Demyk K, Cordier P, Gengembre L, Grimblot J, d'Hdencourt L, Jones AP, Leroux H (2002) Low-energy helium ion irradiation-induced amorphization and chemical changes in olivine: Insights for silicate dust evolution in the interstellar medium. Meteorit Planet Sci 37:1599–1614
Cassidy W, Hapke B (1975) Effects of darkening processes on surfaces of airless bodies. Icarus 25:371–383
Chamberlin S, Christoffersen R, Keller L (2008) Space plasma Ion processing of the lunar soil: Modeling of radiation-damaged rim widths on lunar grains. Lunar Planet Sci 36:2302
Christoffersen R, Keller LP (2015) Solar ion processing of Itokawa grains: Constraints on surface exposure times. Lunar Planet Sci 46:2084
Christoffersen R, McKay DS, Keller LP (1996) Microstructure, chemistry, and origin of grain rims on ilmenite from the lunar soil finest fraction. Meteorit Planet Sci 31:835–848
Christoffersen R, Keller LP, Dukes C, Rahman Z, Baragiola R (2010a) Experimental investigation of space radiation processing in lunar soil ilmenite: Combining perspectives from surface science and transmission electron microscopy. Lunar Planet Sci 41:1532
Christoffersen R, Dukes C, Keller LP, Baragiola R (2010b) The effect of space radiation processing on the surface chemistry of lunar regolith grains: Experimental constraints. Annu Meeting Meteorit Soc 73:5379
Christoffersen R, Rahman Z, Keller LP (2012) Solar ion sputter deposition in the lunar regolith: experimental simulation using focused-ion beam techniques. Lunar Planet Sci 43:2614
Christoffersen R, Cintala MJ, Keller LP, See TH, Horz F (2013) Nanoscale mineralogy and composition of experimental regolith agglutinates produced under asteroidal impact conditions. Lunar Planet Sci 44:2605
Christoffersen R, Loeffler MJ, Rahman Z, Dukes C, Team I (2017) Experimental hypervelocity dust impacts in olivine: FIB/TEM characterization of micron-scale craters with comparison to natural and laser-simulated small-scale impact effects. Lunar Planet Sci 48:2578
Cintala MJ (1992) Impact-induced thermal effects in the lunar and Mercurian regoliths. J Geophys Res 97:947–973
Cintala MJ, Hörz F (1988) The effects of impact velocity on the evolution of experimental regoliths. Lunar Planet Sci 18:409–422
Clark BE, Lucey P, Helfenstein P, Bell JF, Peterson C, Veverka J, McConnochie T, Robinson MS, Bussey B, Murchie SL, Izenberg NI (2001) Space weathering on Eros: Constraints from albedo and spectral measurements of Psyche crater. Meteorit Planet Sci 36:1617–1637
Clegg-Watkins RN, Jolliff BL, Boyd A, Robinson MS, Wagner R, Stopar JD, Plescia JB, Speyerer EJ (2016) Photometric characterization of the Chang'e-3 landing site using LROC NAC images. Icarus 273:84–95
Cocks FH (2010) 3He in permanently shadowed lunar polar surfaces. Icarus 206:778–779
Corley L, Gillis-Davis J, Lucey P, Trang D (2016) Space weathering at the lunar poles: The effect of temperature on reflectance of materials weathered by laser irradiation. Lunar Planet Sci 47:2692
Corley LM, Gillis-Davis JJ, Schultz PH (2017a) A comparison of kinetic impact and laser irradiation space weathering experiments. Lunar Planet Sci 48:1721
Corley LM, Gillis-Davis JJ, Lucey PG, Trang D (2017b) The effect of temperature on the reflectance spectra of pyroxene and a highlands analog weathered by laser irradiation. Lunar Planet Sci 48:1698
Costello ES, Ghent RR, Lucey PG (2018) The mixing of the lunar regolith: Vital updates to a canonical model. Icarus 314:327–344
Crites ST, Lucey PG (2015) Revised mineral and Mg# maps of the Moon from integrating results from the Lunar Prospector neutron and gamma-ray spectrometers with Clementine spectroscopy. Am Mineral 100:973–982
Denevi BW, Lucey PG, Sherman SB (2008) Radiative transfer modeling of near-infrared spectra of lunar mare soils: Theory and measurement. J Geophys Res 113:E02003

Denevi BW, Robinson MS, Boyd AK, Sato H, Hapke BW, Hawke BR (2014) Characterization of space weathering from Lunar Reconnaissance Orbiter Camera ultraviolet observations of the Moon. J Geophys Res: Planets 119:976–997

Denevi BW, Robinson MS, Boyd AK, Blewett DT, Klima RL (2016) The distribution and extent of lunar swirls. Icarus 273: 53–67

Domingue DL, Chapman CR, Killen RM, Zurbuchen TH, Gilbert JA, Sarantos M, Benna M, Slavin JA, Schriver D, Trávníček PM, Orlando TMc(2014) Mercury's weather-beaten surface: Understanding Mercury in the context of lunar and asteroidal space weathering studies. Space Sci Rev 181:121–214

Domingue DL, Vilas F, Choo T, Stockstill-Cahill KR, Cahill JTS, Hendrix AR (2016) Regional spectrophotometric properties of 951 Gaspra. Icarus 280:340–358

Dran JC, Durrieu L, Jouret C, Maurette M (1970) Habit and texture studies of lunar and meteoritic materials with a 1 MeV electron microscope. Earth Planet Sci Lett 9:391–400

Ehlmann BL, Klima RL, Bennett CL, Blaney D, Bowles N, Calcutt S, Dickson J, Donaldson Hanna K, Edwards CS, Green R O, Greenberger RN (2022) Lunar Trailblazer: A pioneering SmallSat for lunar water and lunar geology. Lunar Planet Sci 53:2316

El-Baz F (1972) The Alhazen to Abul Wafa Swirl Belt: An extensive field of light-colored sinuous markings. *In:* Apollo 16: Preliminary Science Report. NASA Spec Publ SP 315, p 29–93

Emery BA, Richardson IG, Evans DS, Rich FJ (2009) Solar wind structure sources and periodicities of auroral electron power over three solar cycles. J Atmos Sol Terr Phys 71:1157–1175

Evans LG, Peplowski PN, Rhodes EA, Lawrence DJ, McCoy TJ, Nittler LR, Solomon SC, Sprague AL, Stockstill-Cahill KR, Starr RD, Weider SZ (2012) Major-element abundances on the surface of Mercury: Results from the MESSENGER Gamma-Ray Spectrometer. J Geophys Res 117:E00L07

Fa W, Jin Y-Q (2007) Quantitative estimation of helium-3 spatial distribution in the lunar regolith layer Icarus 190:15–23

Farrell WM, Halekas JS, Horányi M, Killen RM, Grava C, Szalay JR, Benna M, Clark PE, Collier MR, Colaprete A, Deca J, Elphic RC, Fatemi S, Futaana Y, Holmström M, Hurley DM, Kramer GY, Mahaffy PR, Nishino MN, Noble SK, Saito Y, Poppe AR, Retherford KD, Wang X, Yokota S (20XX) The Dust, Atmosphere, and Plasma at the Moon. Rev Mineral Geochem xx:xx-xx

Fazio A, Harries D, Matthäus G, Mutschke H, Nolte S, and Langenhorst F (2018) Femtosecond laser irradiation of olivine single crystals: Experimental simulation of space weathering Icarus 299:240–252

Feynman J, Armstrong TP, Dao-Gibner L, Silverman, S (1990) New interplanetary proton fluence model. J Spacecraft Rockets 27:403–410

Fiege K, Guglielmino M, Altobelli N, Trieloff M, Srama R, Orlando TM (2019) Space weathering induced via microparticle impacts: 2 Dust impact simulation and meteorite target analysis. J Geophys Res: Planets 124:1084–1099

Fischer EM, Pieters CM (1994) Remote determination of exposure degree and iron concentration of lunar soils using VIS-NIR spectroscopic methods. Icarus 111:475–488

Fisher EA, Lucey PG, Lemelin M, Greenhagen BT, Siegler MA, Mazarico E, Aharonson O, Williams JP, Hayne PO, Neumann GA, Paige DA (2017) Evidence for surface water ice in the lunar polar regions using reflectance measurements from the Lunar Orbiter Laser Altimeter and temperature measurements from the Diviner Lunar Radiometer Experiment. Icarus 292:74–85

Fleischer RL, Price PB, Walker RM (1975) Nuclear Tracks in Solids. University of California Press, Berkeley

Fu RR, Weiss BP, Shuster DL, Gattacceca J, Grove TL, Suavet C, Lima EA, Li L, Kuan AT (2012) An ancient core dynamo in asteroid Vesta. Science 338:238–241

Futaana Y, Machida S, Saito Y, Matsuoka A, Hayakawa H (2003) Moon-related nonthermal ions observed by Nozomi: Species, sources, and generation mechanisms. J Geophys Res 108:1025

Futaana Y, Barabash S, Wieser M, Lue C, Wurz P, Vorburger A, Bhardwaj A, Asamura K (2013) Remote energetic neutral atom imaging of electric potential over a lunar magnetic anomaly. Geophys Res Lett 40:262–266

Garrick-Bethell I, Head JW, Pieters CM (2011) Spectral properties, magnetic fields, and dust transport at lunar swirls. Icarus 212:480–492

Gault DE, Hörz F, Brownlee DE, Hartung JB (1974) Mixing of the lunar regolith. Proc Lunar Planet Sci Conf 5:2365–2386

Gay P, Bancroft GM, Bown MG (1970) Diffraction and mossbauer studies of minerals from lunar soils and rocks. Science 167:626–628

Ghent RR, Leverington DW, Campbell BA, Hawke BR, Campbell DB (2005) Earth-based observations of radar-dark crater haloes on the Moon: Implications for regolith properties. J Geophys Res 110:E02005

Ghent RR, Hayne PO, Bandfield JL, Campbell BA, Allen CC, Carter LM, Paige DA (2014) Constraints on the recent rate of lunar ejecta breakdown and implications for crater ages. Geology 42:1059–1062

Gibson EK Jr. Bustin R (1987) Hydrogen abundances vs depth in the lunar regolith: results from an Apollo 15 Double drive tube and deep drill core. Lunar Planet Sci 18:324

Giguere TA, Hawke BR, Gaddis LR, Blewett DT, Gillis-Davis JJ, Lucey PG, Smith GA, Spudis PD, Taylor GJ (2006) Remote sensing studies of the Dionysius region of the Moon. J Geophys Res 111:E06009

Gladstone GR, Retherford KD, Egan AF, Kaufmann DE, Miles PF, Parker JW, Horvath D, Rojas PM, Versteeg MH, Davis MW, Greathouse TK (2012) Far-ultraviolet reflectance properties of the Moon's permanently shadowed regions. J Geophys Res 117:E00H04

Glotch TD, Bandfield JL, Lucey PG, Hayne PO, Greenhagen BT, Arnold JA, Ghent RR, Paige DA (2015) Formation of lunar swirls by magnetic field standoff of the solar wind. Nat Commun 6:6189
Gold T (1955) The Lunar Surface. Mon Not R Astron Soc 115:585–604
Gosling JT (1993) The solar flare myth. J Geophys Res, Space Physics 98: 18937–18949
Gravnik M, Morbidelli A, Jedicke R, Bolin B, Bottke WF, Behosre E, Vokrouhlický D, Delbò M, Michel P (2016) Super-catastrophic disruption of asteroids at small perihelion distances. Nature 530: 303–306
Greenhagen BT, Lucey PG, Wyatt MB, Glotch TD, Allen CC, Arnold JA, Bandfield JL, Bowles NE, Hanna KL, Hayne PO, Song E (2010) Global silicate mineralogy of the Moon from the Diviner lunar radiometer. Science 329:1507–1509
Grier JA, McEwen AS, Lucey PG, Milazzo M, Strom RG (2001) Optical maturity of ejecta from large rayed lunar craters. J Geophys Res: Planets 106:32847–32862
Greer J, Rout SS, Isheim D, Seidman DN, Wieler R, Heck PR (2020) Atom probe tomography of space-weathered lunar ilmenite grain surfaces. Meteorit Planet Sci 55:426–440
Gross J, Gillis-Davis J, Isaacson P, Le L (2015) How rich is rich? Placing constraints on the abundance of spinel in the pink spinel anorthosite lithology on the Moon through space weathering. Lunar Planet Sci 46:2642
Grün E, Horanyi M, Sternovsky Z (2011) The lunar dust environment. Planet Space Sci 59:1672–1680
Halekas JS, Bale SD, Mitchell DL, Lin RP (2005) Electrons and magnetic fields in the lunar plasma wake. J Geophys Res 110:A07222
Halekas JS, Delory GT, Brain DA, Lin RP, Mitchell DL (2008) Density cavity observed over a strong lunar crustal magnetic anomaly in the solar wind: A mini-magnetosphere? Planet Space Sci 56:941–946
Hapke B (2022) Do deep electrical discharges initiated by solar energetic particle events occur in the lunar regolith? Icarus 372:114758
Hapke B (2001) Space weathering from Mercury to the asteroid belt. J Geophys Res: Planets 106:10039–10073
Hapke B (2011) Theory of Reflectance and Emittance Spectroscopy. 2nd ed. Cambridge University Press, Cambridge
Hapke B, Cassidy W, Wells E, Bernatowicz TJ, Nichols RH Jr, Hohenberg CM, Maurette M, Keller LP, McKay DS (1994) Vapor Deposits in the Lunar Regolith. Science 264:1779–1780
Hapke B, Cassidy W, Wells E (1975) Effects of vapor-phase deposition processes on the optical, chemical, and magnetic properties of the lunar regolith. Moon 13:339–353
Hapke BW, Cohen AJ, Cassidy WA, Wells EN (1970) Solar radiation effects in lunar samples. Science 167: 745–747
Hartmann WK (1977) Relative crater production rates on planets. Icarus 31:260–276
Hawke BR, Blewett DT, Lucey PG, Smith GA, Bell JF, Campbell BA, Robinson MS (2004) The origin of lunar crater rays. Icarus 170:1–16
Hawke BR, Gillis JJ, Giguere TA, Blewett DT, Lawrence DJ, Lucey PG, Smith GA, Spudis PD, Taylor GJ (2005) Remote sensing and geologic studies of the Balmer–Kapteyn region of the Moon. J Geophys Res 110:E06004
Heldmann JL, Lamb J, Asturias D, Colaprete A, Goldstein DB, Trafton LM, Varghese PL (2015) Evolution of the dust and water ice plume components as observed by the LCROSS visible camera and UV–visible spectrometer. Icarus 254:262–275
Hemingway D, Garrick-Bethell I (2012) Magnetic field direction and lunar swirl morphology: Insights from Airy and Reiner Gamma. J Geophys Res: Planets 117:E10012
Hemingway DJ, Garrick-Bethell I, Kreslavsky MA (2015) Latitudinal variation in spectral properties of the lunar maria and implications for space weathering. Icarus 261:66–79
Hendrix AR, Vilas F (2006) The effects of space weathering at UV wavelengths: S-class asteroids. Astron J 132:1396–1404
Hendrix AR, Retherford KD, Randall Gladstone G, Hurley DM, Feldman PD, Egan AF, Kaufmann DE, Miles PF, Parker JW, Horvath D, Rojas PM (2012) The lunar far-UV albedo: Indicator of hydration and weathering. J Geophys Res: Planets 117:E12001
Hendrix AR, Greathouse TK, Retherford KD, Mandt KE, Gladstone GR, Kaufmann DE, Hurley DM, Feldman PD, Pryor WR, Stern SA, Cahill JT (2016) Lunar swirls: Far-UV characteristics. Icarus 273:68–74
Hiroi T, Abe M, Kitazato K, Abe S, Clark BE, Sasaki S, Ishiguro M, Barnouin-Jha OS (2006) Developing space weathering on the asteroid 25143 Itokawa. Nature 443:56–58
Hood LL, Schubert G (1980) Lunar magnetic anomalies and surface optical properties. Science 208:49–51
Hood LL, Williams CR (1989) The lunar swirls - Distribution and possible origins. Lunar Planet Sci 19:99–113
Horanyi M, Szalay J, Kempf S, Schmidt J, Grün E, Srama R, Sternovsky Z (2015) A permanent, asymmetric dust cloud around the Moon. Nature 522:324–326
Hörz F, Cintala M, See TH, Cardenas F, Thompson TD (1984) Grain size evolution and fractionation trends in an experimental regolith. Lunar Planet Sci 15:183–196
Housley RM, Grant RW, Abdel-Gawad M (1972) Study of excess Fe metal in the lunar fines by magnetic separation: Mössbauer spectroscopy, and microscopic examination. Proc Lunar Sci 3:1065–1076
Housley R, Cirlin EH, Grant RW (1973) Origin and characteristics of excess Fe metal in lunar glass welded aggregates. Proc Lunar Sci Conf 4:2737–2750
Housley RM, Cirlin EH, Paton NE, Goldberg IB (1974) Solar wind and micrometeorite alteration of the lunar regolith. Proc Lunar Planet Sci Conf 5:2623–2642
Hundhausen A J (1972) Coronal Expansion and Solar Wind. Springer-Verlag, New York

Hurley DM, Farrell WM (2013) Solar wind fluency to the lunar surface. Lunar Planet Sci 44:2015
Ishiguro M, Hiroi T, Tholen DJ, Sasaki S, Ueda Y, Nimura T, Abe M, Clark BE, Yamamoto A, Yoshida F, Nakamura R (2007) Global mapping of the degree of space weathering on asteroid 25143 Itokawa by Hayabusa/AMICA observations. Meteorit Planet Sci 42:1791–1800
James C, Letsinger S, Basu A, Wentworth SJ, McKay DS (2002) Size distribution of Fe globules in lunar agglutinitic glass. Lunar Planet Sci 33:1827
Jewitt D (2013) Properties of near-sun asteroids. Astron J 145:133
Jewitt D, Li J J (2010) Activity in Geminid Parent (3200) Phaethon. Astron J 140:1519–1527
Johnson RE (1990) Energetic Charged-Particle Interactions with Atmospheres and Surfaces. Springer-Verlag, Berlin
Johnson JR, Swindle TD, Lucey PG (1999) Estimated solar wind-implanted helium-3 distribution on the Moon. Geophys Res Lett 26:385–388
Jones J, Brown P (1993) Sporadic meteor radiant distributions—Orbital survey 2084 results. Mon Not R Astron Soc 265:2085
Jordan AP, Stubbs TJ, Joyce CJ, Schwadron NA, Spence HE, Wilson JK (2013) The formation of molecular hydrogen from water ice in the lunar regolith by energetic charged particles. J Geophys Res: Planets 118:1257–1264
Jordan AP, Stubbs TJ, Wilson JK, Hayne PO, Schwadron NA, Spence HE, Izenberg NR (2017a) How dielectric breakdown may weather the lunar regolith and contribute to the lunar exosphere. Lunar Planet Sci 48:2332
Jordan AP, Stubbs TJ, Wilson JK, Schwadron NA, Spence HE (2017b) The rate of dielectric breakdown weathering of lunar regolith in permanently shadowed regions. Icarus 283:352–358
Kaluna HM, Gillis-Davis JJ (2017) Contexting experimental space weathering with lunar soil maturity. Lunar Planet Sci 48:2540
Kanuchova Z, Brunetto R, Fulvio D, Strazzulla G (2015) Near-ultraviolet bluing after space weathering of silicates and meteorites. Icarus 258:289–296
Kaydash V, Kreslavsky M, Shkuratov Y, Gerasimenko S, Pinet P, Josset J-L, Beauvivre S, Foing, B (2009) Photometric anomalies of the lunar surface studied with SMART-1 AMIE data. Icarus 202:393–413
Keller LP, Berger, EL (2014) Space weathering of olivine in lunar soils: A comparison to Itokawa regolith samples. Ann Meeting Meteorit Soc 77:5088
Keller LP, Clemett SJ (2001) Formation of nanophase iron in the lunar regolith. Lunar Planet Sci 32:1762
Keller LP, McKay DS (1993) Discovery of vapor deposits in the lunar regolith. Science 261:1305–1307
Keller LP, McKay DS (1997) The nature and origin of rims on lunar soil grains. Geochim Cosmochim Acta 61:2331–2341
Keller LP, Zhang S (2015) Rates of space weathering in lunar soils. Space Weathering of Airless Bodies Workshop, Abs #2056
Keller LP, Wentworth SJ, McKay DS (1998) Space weathering: Reflectance spectroscopy and TEM analysis of individual lunar grains. Lunar Planet Sci 29:1762
Keller LP, Berger EL, Zhang S, Christoffersen R (2021) Solar energetic particle tracks in lunar samples: A transmission electron microscope calibration and implications for lunar space weathering. Meteorit Planet Sci 56:1685–1707
Kennel CF, Lanzerotti LJ, Parker EN (1979) Solar system plasma physics. North-Holland, Amsterdam
Kinczyk MJ, Denevi BW, Boyd AK, Clegg-Watkins RN, Hapke BW, Henriksen MR, Robinson MS, Sato H (2016) Controls on the photometric properties of lunar swirls in comparison to fresh crater ejecta. Lunar Planet Sci 47:2343
Kissel J, Krueger FR (1987) Ion formation by impact of fast dust particles and comparison with related techniques. Appl Phys A 42:69–85
Kohout T, Čuda J, Filip J, Britt D, Bradley T, Tuček J, Skála R, Kletetschka G, Kašlík J, Malina O, Šišková K (2014) Space weathering simulations through controlled growth of iron nanoparticles on olivine. Icarus 237:75–83
Kramer GY, Combe J-P, Harnett EM, Hawke BR, Noble SK, Blewett DT, McCord TB, Giguere TA (2011a) Characterization of lunar swirls at Mare Ingenii: A model for space weathering at magnetic anomalies. J Geophys Res 116:E04008
Kramer GY, Besse S, Dhingra D, Nettles J, Klima R, Garrick-Bethell I, Clark RN, Combe JP, Head III JW, Taylor LA, Pieters CM (2011b) M3 spectral analysis of lunar swirls and the link between optical maturation and surface hydroxyl formation at magnetic anomalies. J Geophys Res 116:E00G18
Kreslavsky MA, Shkuratov YG (2003) Photometric anomalies of the lunar surface: Results from Clementine data. J Geophys Res 108(E3):5015
Kuhlman KR, Sridharan K, Kvit A (2015) Simulation of solar wind space weathering in orthopyroxene. Planet Space Sci 115:110–114
Kumar PA, Kumar S (2014) Estimation of optical maturity parameter for lunar soil characterization using Moon Mineralogy Mapper (M3). Adv Space Res 53:1694–1719
Kurahashi E, Yamanaka C, Nakamura K, Sasaki S (2002) Laboratory simulation of space weathering: ESR measurements of nanophase metallic iron in laser-irradiated materials. Earth Planets Space 54:E5–E7
Laczniak DL, Thompson, MS, Christoffersen, R, Dukes, CA, Clemett, SJ, Morris, RV and Keller LP (2021) Characterizing the spectral, microstructural, and chemical effects of solar wind irradiation on the Murchison carbonaceous chondrite through coordinated analyses. Icarus 364:114479

Lemelin M, Lucey PG, Gaddis LR, Hare T, Ohtake M (2016a) Global map products from the Kaguya Multiband Imager at 512 PPD: Minerals, FeO, and OMAT. Lunar Planet Sci 47:2994
Lemelin M, Lucey PG, Neumann GA, Mazarico EM, Barker MK, Kakazu A, Trang D, Smith DE, Zuber MT (2016b) Improved calibration of reflectance data from the LRO Lunar Orbiter Laser Altimeter (LOLA) and implications for space weathering. Icarus 273:315–328
Liu Y, Guan Y, Zhang Y, Rossman GR, Eiler JM Taylor LA (2012) Direct measurement of hydroxyl in the lunar regolith and the origin of lunar surface water. Nat Geosci 5:779–782
Loeffler MJ, Dukes CA, Baragiola RA (2009) Irradiation of olivine by 4 keV He^+: Simulation of space weathering by the solar wind. J Geophys Res: Planets 114:E03003
Loeffler MJ, Dukes CA, Christoffersen R, Baragiola RA (2016) Space weathering of silicates simulated by successive laser irradiation: In situ reflectance measurements of Fo_{90}, Fo_{99}, and SiO_2. Meteorit Planet Sci 51:261–275
Logan LM, Hunt GR, Salisbury JW, Balsamo SR (1973) Compositional implications of Christiansen frequency maximums for infrared remote sensing applications. J Geophys Res 78:4983–5003
Love SG, Brownlee DE (1993) A direct measurement of the terrestrial mass accretion rate of cosmic dust. Science 262:550–553
Lucey P, Noble S (2008) Experimental test of a radiative transfer model of the optical effects of space weathering. Icarus 197:348–353
Lucey PG (2004) Mineral maps of the Moon. Geophys Res Lett 31:L08701
Lucey PG, Riner MA (2011) The optical effects of small iron particles that darken but do not redden: Evidence of intense space weathering on Mercury. Icarus 212:451–462
Lucey PG, Blewett DT, Taylor GJ, Hawke BR (2000) Imaging of lunar surface maturity. J Geophys Res: Planets 105:20377–20386
Lucey PG, Neumann GA, Riner MA, Mazarico E, Smith DE, Zuber MT, Paige DA, Bussey DB, Cahill JT, McGovern A, Isaacson P (2014) The global albedo of the Moon at 1064 nm from LOLA. J Geophys Res: Planets 119:1665–1679
Lucey PG, Greenhagen BT, Song E, Arnold JA, Lemelin M, Hanna KD, Bowles NE, Glotch TD, Paige DA (2017) Space weathering effects in Diviner Lunar Radiometer multispectral infrared measurements of the lunar Christiansen Feature: Characteristics and mitigation. Icarus 283: 343–351
Lucey PG, Costello ES, Ghent RR, Li S (2018) Ice distribution at the poles of the Moon and Mercury: The role of regolith overturn. Lunar Planet Sci 49:1678
Lue C, Futaana Y, Barabash S, Wieser M, Holmström M, Bhardwaj A, Dhanya MB, Wurz P (2011) Strong influence of lunar crustal fields on the solar wind flow. Geophys Res Lett 38:L03202
Mahanti P, Denevi BW, Robinson MS (2016) On the spatial and age based variation of optical maturity for Copernican craters. Annu Meeting Lunar Exploration Analysis Group Abs # 5064
Mao HK, Virgo D, Bell PM (1973) Analytical and experimental study of iron and titanium in orange glass from Apollo 17 soil sample 74220. Proc Lunar Sci Conf 4:397–412
McCord TB, Adams JB, Johnson TV (1970) Asteroid Vesta: Spectral reflectivity and compositional implications. Science 168:1445–1447
McKay DS, Basu A (1983) The production curve for agglutinates in planetary regoliths. J Geophys Res 88:B193–B199
Meyer FW, Harris PR, Taylor CN, Meyer HM, Barghouty AF, and Adams JH (2011) Sputtering of lunar regolith simulant by protons and singly and multicharged Ar ions at solar wind energies. Nucl Instrum Methods Sect B 269:1316–1320
Molaro JL, Byrne S, Le J-L (2017) Thermally induced stresses in boulders on airless body surfaces, and implications for rock breakdown. Icarus 294:247–261
Moroz LV, Fisenko AV, Semjonova LF, Pieters CM, Korotaeva NN (1996) Optical effects of regolith processes on S-asteroids as simulated by laser shots on ordinary chondrite and other mafic materials. Icarus 122:366–382
Morris RV (1976) Surface exposure indices of lunar soils—A comparative FMR study. Proc Lunar Planet Sci 7:315–335
Morris RV (1977) Origin and evolution of the grain-size dependence of the concentration of fine-grained metal in lunar soils: The maturation of lunar soils to a steady-state stage. Proc Lunar Planet Sci 8:3719–3747
Morris RV (1978) The surface exposure/maturity/of lunar soils-Some concepts and Is/FeO compilation. Proc Lunar Planet Sci 9:2287–2297
Morris RV (1980) Origins and size distributions of metallic iron particles in the lunar regolith. Lunar Planet Sci 11:1697–1712
Morris RV, Klingelhöfer G, Korotev RL, Shelfer TD (1998) Mössbauer mineralogy on the Moon: The lunar regolith. Hyperfine Interactions 117:405–432
Murchie SL, Klima RL, Denevi BW, Ernst CM, Keller MR, Domingue DL, Blewett DT, Chabot NL, Hash CD, Malaret E, Izenberg NR (2015) Orbital multispectral mapping of Mercury with the MESSENGER Mercury Dual Imaging System: Evidence for the origins of plains units and low-reflectance material. Icarus 254:287–305
Nakamura T, Noguchi T, Tanaka M, Zolensky ME, Kimura M, Tsuchiyama A, Nakato A, Ogami T, Ishida H, Uesugi M, Yada T (2011) Itokawa dust particles: a direct link between S-type asteroids and ordinary chondrites. Science 333:1113–1116

Nash DB, Conel JE (1973) Vitrification darkening of rock powders: Implications for optical properties of the lunar surface. Moon 8:346–364
Nash DB, Salisbury JW, Conel JE, Lucey PG, Christensen PR (1993) Evaluation of infrared emission spectroscopy for mapping the Moon's surface composition from lunar orbit. J Geophys Res 98(E12):23535–23552
Neish CD, Blewett DT, Bussey DBJ, Lawrence SJ, Mechtley M, Thomson BJ (2011) The surficial nature of lunar swirls as revealed by the Mini-RF instrument. Icarus 215:186–196
Nesvorný D, Jenniskens P, Levison HF, Bottke WF, Vokrouhlický D, Gounelle M (2010) Cometary origin of the zodiacal cloud and carbonaceous micrometeorites. Implications for hot debris disks .Astrophys J 713:816–836
Nesvorný D, Vokrouhlický D, Pokorný P Janches D (2011) Dynamics of dust particles released from Oort Cloud Comets and their contribution to radar meteors. Astrophys J 743:37
Nettles JW, Staid M, Besse S, Boardman J, Clark RN, Dhingra D, Isaacson P, Klima R, Kramer G, Pieters CM, Taylor LA (2011) Optical maturity variation in lunar spectra as measured by Moon Mineralogy Mapper data. J Geophys Res 116:E00G17
Nichols RH Jr, Hohenberg CM, Olinger CT (1994) Implanted solar helium, neon, and argon in individual lunar ilmenite grains: surface effects and a temporal variation in the solar wind composition. Geochim Cosmochim Acta 58:1031–1042
Nishino MN, Fujimoto M, Maezawa K, Saito Y, Yokota S, Asamura K, Tanaka T, Tsunakawa H, Matsushima M, Takahashi F, Terasawa T (2009) Solar-wind proton access deep into the near-Moon wake. Geophys Res Lett 36:L16103
Nittler LR, Starr RD, Lim L, Mccoy TJ, Burbine TH, Reedy RC, Trombka JI, Gorenstein P, Squyres SW, Boynton WV, Mcclanahan TP (2001) X-ray fluorescence measurements of the surface elemental composition of asteroid 433 Eros. Meteorit Planet Sci 36:1673–1695
Noble SK, Pieters CM (2003) Space weathering on Mercury: Implications for remote sensing. Sol Sys Res 37:31–35
Noble SK, Pieters CM, Taylor LA, Morris RV, Allen CC, McKay DS, Keller LP (2001) The optical properties of the finest fraction of lunar soil: Implications for space weathering. Meteorit Planet Sci 36:31–42
Noble SK, Pieters CM, Keller LP (2007) An experimental approach to understanding the optical effects of space weathering. Icarus 192:629–642
Noble SK, Keller LP, Pieters CM (2011) Evidence of space weathering in regolith breccias II: Asteroidal regolith breccias. Meteorit Planet Sci 45:2007–2015
Noble SK, Hiroi T, Keller LP, Rahman Z, Sasaki S, Pieters CM (2011) Experimental space weathering of ordinary chondrites by nanopulse laser: TEM results. Lunar Planet Sci 42:1382
Noble SK, Keller LP, Christoffersen R, Rahman Z (2016) The microstructure of lunar micrometeorite impact craters. Lunar Planet Sci 47:1465
Noguchi T, Nakamura T, Kimura M, Zolensky ME, Tanaka M, Hashimoto T, Konno M, Nakato A, Ogami T, Fujimura A, Abe M (2011) Incipient space weathering observed on the surface of Itokawa dust particles. Science 333:1121–1125
Noguchi T, Kimura M, Hashimoto T, Konno M, Nakamura T, Zolensky ME, Okazaki R, Tanaka M, Tsuchiyama A, Nakato A, Ogami T (2013 =2014?) Space weathered rims found on the surfaces of the Itokawa dust particles. Meteorit Planet Sci 49:188–214
Paige DA, Siegler MA, Zhang JA, Hayne PO, Foote EJ, Bennett KA, Vasavada AR, Greenhagen BT, Schofield JT, McCleese DJ, Foote MC (2010a) Diviner Lunar Radiometer observations of cold traps in the Moon's south polar region. Science 330:479–482
Paige DA, Foote MC, Greenhagen BT, Schofield JT, Calcutt S, Vasavada AR, Preston DJ, Taylor FW, Allen CC, Snook KJ, Jakosky BM (2010b) The Lunar Reconnaissance Orbiter Diviner Lunar Radiometer Experiment. Space Sci Rev 150:125–160
Paruso D, Cassidy W, Hapke B (1978) An experimental investigation of fractionation by sputter deposition. Proc Lunar Planet Sci 9:1711–1724
Peplowski PN, Lawrence DJ, Evans LG, Klima RL, Blewett DT, Goldsten JO, Murchie SL, McCoy TJ, Nittler LR, Solomon SC, Starr RD (2015) Constraints on the abundance of carbon in near-surface materials on Mercury: Results from the MESSENGER Gamma-Ray Spectrometer. Planet Space Sci 108:98–107
Pieters CM (1977) Characterization of lunar mare basalt types - II: Spectral classification of fresh mare craters. Proc Lunar Sci Conf 8:1037–1048
Pieters CM, Noble SK (2016) Space weathering on airless bodies. J Geophys Res: Planets 121:1865–1884
Pieters CM, Fischer EM, Rode O, Basu A (1993) Optical effects of space weathering: The role of the finest fraction. J Geophys Res 98:20817–20824
Pieters CM, Ammannito E, Blewett DT, Denevi BW, De Sanctis MC, Gaffey MJ, Le Corre L, Li JY, Marchi S, McCord TB, McFadden LA (2012) Distinctive space weathering on Vesta from regolith mixing processes. Nature 491:79–82
Pieters CM, Garrick-Bethell I, Hemingway D (2014) Magnetic sorting of the regolith on the Moon: Lunar Swirls. AGU Fall Meeting Abs. P11D–10
Pillinger CT (1979) Solar-wind exposure effects in the lunar soil. Rep Prog Phys 42:897–961

Pinet PC, Shevchenko VV, Chevrel SD, Daydou Y, Rosemberg C (2000) Local and regional lunar regolith characteristics at Reiner Gamma Formation: Optical and spectroscopic properties from Clementine and Earth-based data. J Geophys Res 105:9457–9475

Pokorný P, Vokrouhlický D, Nesvorný D, Campbell-Brown M, Brown P (2014) Dynamical model for the toroidal sporadic meteors. Astrophys J 789:25

Poppe AR, Fatemi S, Garrick-Bethell I, Hemingway D, Holmström M (2016) Solar wind interaction with the Reiner Gamma crustal magnetic anomaly: Connecting source magnetization to surface weathering. Icarus 266:261–266

Poppe AR, Farrell WM, Halekas JS (2018) Formation timescales of amorphous rims on lunar grains derived from ARTEMIS observations. J Geophys Res: Planets 123:37–46

Prettyman TH (2014) Chapter 54—Remote sensing of chemical elements using nuclear spectroscopy *In:* Spohn T, Breuer D, Johnson TV (eds) Encyclopedia of the Solar System (Third Edition), Elsevier, Boston, p 1161–1183

Ravishankar A Michałek G (2019) Estimation of arrival time of coronal mass ejections in the vicinity of the earth using *SOlar and Heliospheric Observatory* and *Solar TErrestrial RElations Observatory* observations. Sol Phys 294:125

Reames DV (1999) Particle acceleration at the Sun and in the heliosphere. Space Sci Rev 90:413–491

Reisenfeld DB, Wiens RC, Barraclough BL, Steinberg JT, Neugebauer M, Raines J, Zurbuchen TH (2013) Solar wind conditions and composition during the Genesis Mission as measured by in situ spacecraft. Space Sci Rev 175:125–164

Robinson MS, Hapke BW, Garvin JB, Skillman D, Bell JF III, Ulmer MP, Pieters CM (2007) High resolution mapping of TiO_2 abundances on the Moon using the Hubble Space Telescope. Geophys Res Lett 34:L13203

Saito Y, Yokota S, Tanaka T, Asamura K, Nishino MN, Fujimoto M, Tsunakawa H, Shibuya H, Matsushima M, Shimizu H (2008) Solar wind proton reflection at the lunar surface: Low energy ion measurement by MAP-PACE onboard SELENE (KAGUYA). Geophys Res Lett 35:L24205

Saito Y, Nishino MN, Fujimoto M, Yamamoto T, Yokota S, Tsunakawa H, Shibuya H, Matsushima M, Shimizu H, Takahashi F (2012) Simultaneous observation of the electron acceleration and ion deceleration over lunar magnetic anomalies. Earth Planets Space 64:83–92

Salisbury JW, Walter LS (1989) Thermal infrared (25–135 μm) spectroscopic remote sensing of igneous rock types on particulate planetary surfaces. J Geophys Res 94:9192–9202

Salisbury JW, Basu A, Fischer EM (1997) Thermal infrared spectra of lunar soils. Icarus 130:125–139

Sasaki S, Nakamura K, Hamabe Y, Kurahashi E, Hiroi T (2001) Production of iron nanoparticles by laser irradiation in a simulation of lunar-like space weathering. Nature 410:555–557

Sasaki S, Kurahashi E, Yamanaka C, Nakamura K (2003) Laboratory simulation of space weathering: Changes of optical properties and TEM/ESR confirmation of nanophase metallic iron. Adv Space Res 31:2537–2542

Schmitt HH (2006) Return to the Moon, Copernicus-Praxis, New York

Schultz PH, Srnka LJ (1980) Cometary collisions on the Moon and Mercury. Nature 284:22–26

See TH, Hörz F (1988) Formation of agglutinate-like particles in an experimental regolith. Lunar Planet Sci 18:423–434

Shirley KA (2018) The effects of particle size and albedo on mid-infrared spectroscopy for the Moon, PhD Dissertation Stony Brook University, Stony Brook, NY

Shirley KA, Glotch TD, Yang Y, Jiang T, Zhang H (2017) Synthetic space weathering effects in the near- and mid-infrared. Lunar Planet Sci 48:2115

Shoemaker EM, Hackman RJ (1960) Stratigraphic basis for a lunar time scale. Symp Int Astron Union 14:289–300

Shu A, Collette A, Drake K, Grün E, Horányi M, Kempf S, Mocker A, Munsat T, Northway P, Srama R, Sternovsky Z (2012) 3 MV hypervelocity dust accelerator at the Colorado Center for Lunar Dust and Atmospheric Studies. Rev Sci Instrum 83:075108

Sim CK, Kim SS, Lucey PG, Garrick-Bethell I, Choi Y-J (2017) Asymmetric space weathering on lunar crater walls. Geophys Res Lett 44:11,273–11,281

Simpson JA (1983) Introduction to the galactic cosmic radiation. *In*: Shapiro MM (ed) Composition and origin of cosmic rays, Reidel, Amsterdam, p 1–24

Slyuta EN, Yakovlev OI, Voropaev SA, Dubrovskii AV (2013) He implantation and concentrations in minerals and lunar regolith particles. Geochem Int 51:959–967

Smart DF, Shea MA (1985) A simplified model for timing the arrival of solar flare-initiated shocks. J Geophys Res Space Phys 90:183–190

Speyerer EJ, Povilaitis RZ, Robinson MS, Thomas PC, Wagner RV (2016) Quantifying crater production and regolith overturn on the Moon with temporal imaging. Nature 538:215–218

Staid MI, Pieters CM (2000) Integrated spectral analysis of mare soils and craters: Applications to eastern nearside basalts. Icarus 145:122–139

Sun L, Ling Z, Zhang J, Li B, Chen J, Wu Z, Liu J (2016) Lunar iron and optical maturity mapping: Results from partial least squares modeling of Chang'E-1 IIM data. Icarus 280:183–198

Szalay JR, Horányi M (2015) Annual variation and synodic modulation of the sporadic meteoroid flux to the Moon. Geophys Res Lett 42:10,580–10,584

Tang H, Wang S, Li X (2012) Simulation of nanophase iron production in lunar space weathering. Planet Space Sci 60:322–327

Taylor LA, Pieters C M, Keller LP, Morris RV, McKay DS (2001) Lunar mare soils: Space weathering and the major effects of surface-correlated nanophase Fe. J Geophys Res 106:27,985–27,999

Taylor LA, Pieters C, Patchen A, Taylor D-HS, Morris RV, Keller LP, McKay DS (2010) Mineralogical and chemical characterization of lunar highland soils: Insights into the space weathering of soils on airless bodies. J Geophys Res 115:E02992

Thompson MS, Zega TJ Howe JY (2017) In situ experimental formation and growth of Fe nanoparticles and vesicles in lunar soil: Meteorit Planet Sci 52:413–427

Thompson MS, Zega TJ, Becerra P, Keane JT, Byrne S (2016) The oxidation state of nanophase Fe particles in lunar soil: Implications for space weathering. Meteorit Planet Sci 51:1082–1095

Trang D, Lucey PG (2017) Mapping the submicroscopic iron particle abundances across the lunar surface using a radiative transfer model and Kaguya Multiband Imager data. Lunar Planet Sci 48:1042

Trang D, Lucey PG, Izenberg NR (2017) Radiative transfer modeling of MESSENGER VIRS spectra: Detection and mapping of submicroscopic iron and carbon. Icarus 293:206–217

Trang D, Thompson MS, Clark BE, Kaplan HH, Zou XD, Li JY, Ferrone SM, Hamilton VE, Simon AA, Reuter DC, Keller LP (2021) The role of hydrated minerals and space weathering products in the bluing of carbonaceous asteroids. Planet Sci J 2:68

Trombka JI, Squyres SW, Bruckner J, Boynton WV, Reedy RC, McCoy TJ, Gorenstein P, Evans LG, Arnold JR, Starr RD, Nittler LR (2000) The elemental composition of asteroid 433 Eros: Results of the NEAR-Shoemaker X-ray spectrometer. Science 289:2101–2105

Vanzani V, Marzari F, Dotto E (1997) Micrometeoroid impacts on the lunar surface. Lunar Planet Sci 28:1025

Vernazza P, Brunetto R, Strazzulla G, Fulchignoni M, Rochette P, Meyer-Vernet N, Zouganelis I (2006) Asteroid colors: a novel tool for magnetic field detection? The case of Vesta. Astron Astrophys Suppl Ser 451:L43–L46

Vorburger A, Wurz P, Barabash S, Wieser M, Futaana Y, Holmström M, Bhardwaj A, Asamura K (2012) Energetic neutral atom observations of magnetic anomalies on the lunar surface. J Geophys Res 117:A07208

Wang LM Ewing RC (1992) Ion-beam-induced amorphization of complex ceramic materials-minerals. MRS Bull 17:38–44

Wang Z, Wu Y, Blewett DT, Cloutis EA, Zheng Y, Chen J (2017) Submicroscopic metallic iron in lunar soils estimated from the in situ spectra of the Chang'E-3 mission. Geophys Res Lett 44:3485–3492

Weider SZ, Nittler LR, Starr RD, McCoy TJ, Solomon SC (2014) Variations in the abundance of iron on Mercury's surface from MESSENGER X-Ray Spectrometer observations. Icarus 235:170–186

Wells E, Hapke B (1977) Lunar soil: Iron and titanium bands in the glass fraction. Science 195:977–979

Whipple FL (1983) 1983 TB and the Geminid Meteors. IAU Circ 3881

Whitaker EA (1972) Lunar color boundaries and their relationship to topographic features: A preliminary survey. Moon 4:348–355

Wieser M, Barabash S, Futaana Y, Holmström M, Bhardwaj A, Sridharan R, Dhanya MB, Schaufelberger A, Wurz P, Asamura K (2010) First observation of a mini-magnetosphere above a lunar magnetic anomaly using energetic neutral atoms. Geophys Res Lett 37:L05103

Wilhelms DE (1987) The Geologic History of the Moon. US Geol Surv Prof Paper 1348

Williams J-P, Paige DA, Greenhagen BT, Sefton-Nash E (2017) The global surface temperatures of the Moon as measured by the Diviner Lunar Radiometer Experiment. Icarus 283:300–325

Wu Y, Hapke B (2018) Spectroscopic observations of the Moon at the lunar surface. Earth Planet Sci Lett. 484:145–153

Wu Y, Li X, Yao W, Wang S (2017) Impact characteristics of different rocks in a pulsed laser irradiation experiment: Simulation of micrometeorite bombardment on the Moon. J Geophys Res: Planets 122:1956–1967

Yamada M, Sasaki S, Nagahara H, Fujiwara A, Hasegawa S, Yano H, Hiroi T, Ohashi H, Otake H (1999) Simulation of space weathering of planet-forming materials: Nanosecond pulse laser irradiation and proton implantation on olivine and pyroxene samples. Earth Planets Space 51:1255–1265

Yermolaev YI, Nikolaeva NS, Lodkina IG, Yermolaev MY (2012) Geoeffectiveness and efficiency of CIR, sheath, and ICME in generation of magnetic storms. J Geophys Res Space Phys 117:A00L07

Yokota Y, Matsunaga T, Ohtake M, Haruyama J, Nakamura R, Yamamoto S, Ogawa Y, Morota T, Honda C, Saiki K, Nagasawa K (2011) Lunar photometric properties at wavelengths 0.5–16 μm acquired by SELENE Spectral Profiler and their dependency on local albedo and latitudinal zones. Icarus 215:639–660

Zhang S, Keller LP (2010) Formation of ilmenite rims in lunar soils: Vapor deposition, irradiation and thermal effects. Lunar Planet Sci 41:1432

Zimmerman MI, Jackson TL, Farrell WM, Stubbs TJ (2012) Plasma wake simulations and object charging in a shadowed lunar crater during a solar storm. J Geophys Res 117:E00K03.